nature communications

Article

https://doi.org/10.1038/s41467-024-53529-2

Hydrogen radical-boosted electrocatalytic CO_2 reduction using Ni-partnered heteroatomic pairs

Received: 5 July 2023

Accepted: 11 October 2024

Published online: 14 November 2024

Check for updates

Zhibo Yao[1,9], Hao Cheng[2,9], Yifei Xu[3,9], Xinyu Zhan[1], Song Hong[1], Xinyi Tan[4] ✉, Tai-Sing Wu[5], Pei Xiong[6], Yun-Liang Soo[7], Molly Meng-Jung Li[6], Leiduan Hao[1], Liang Xu[1], Alex W. Robertson[8], Bingjun Xu[3], Ming Yang[2] ✉ & Zhenyu Sun[1] ✉

The electrocatalytic reduction of CO_2 to CO is slowed by the energy cost of the hydrogenation step that yields adsorbed *COOH intermediate. Here, we report a hydrogen radical (H•)-transfer mechanism that aids this hydrogenation step, enabled by constructing Ni-partnered hetero-diatomic pairs, and thereby greatly enhancing CO_2-to-CO conversion kinetics. The partner metal to the Ni (denoted as M) catalyzes the Volmer step of the water/proton reduction to generate adsorbed *H, turning to H•, which reduces CO_2 to carboxyl radicals (•COOH). The Ni partner then subsequently adsorbs the •COOH in an exothermic reaction, negating the usual high energy-penalty for the electrochemical hydrogenation of CO_2. Tuning the H adsorption strength of the M site (with Cd, Pt, or Pd) allows for the optimization of H• formation, culminating in a markedly improved CO_2 reduction rate toward CO production, offering 97.1% faradaic efficiency (FE) in aqueous electrolyte and up to 100.0% FE in an ionic liquid solution.

Electrochemical CO_2 reduction (ECR) driven by renewable electricity holds the promise of turning cheap and abundant CO_2 into value-added compounds, while also contributing toward a sustainable and low-carbon future[1–8]. CO produced through a $2e^-$ transfer process appears to be the most likely ECR product to be commercialized. CO is widely used as a key raw material in many important industrial processes, including the water-gas shift reaction, Fischer-Tropsch process, and methanol synthesis[9–13]. The electrochemical transformation of CO_2 to CO can be summarized as three steps[14–16]: (1) $CO_2 + H^+ + e^- \rightarrow$ *COOH; (2) *COOH + $H^+ + e^- \rightarrow$ *CO+ H_2O; (3) *CO → CO + *. The conversion of CO_2 to CO is usually hampered by the first proton-coupled electron transfer (PCET) to form *COOH, which is considered the potential determining step (PDS) with the highest thermodynamic barrier[17–19]. Accelerating the generation and transfer of *H (* denotes an adsorbed site) to CO_2 molecules would be an effective way to enhance the sluggish kinetics of the formation of carbonyl intermediates[20–26]. To this end, constructing an electrocatalyst with dual-active centers would be desirable, where the H adsorption and CO_2 hydrogenation each occur at spatially isolated sites but that are situated within an atomic scale of each other. Optimizing the adsorption of H and CO_2 on separate dual active sites allows one to expedite the reaction kinetics of *COOH formation while concurrently suppressing the competitive hydrogen evolution reaction (HER), thereby expediting the ECR.

[1]State Key Laboratory of Organic–Inorganic Composites, Beijing University of Chemical Technology, Beijing, PR China. [2]Department of Applied Physics, The Hong Kong Polytechnic University, Hung Hom, Hong Kong SAR, PR China. [3]College of Chemistry and Molecular Engineering, Peking University, Beijing, PR China. [4]School of Materials Science and Engineering, Beijing Institute of Technology, Beijing Key Laboratory of Environmental Science and Engineering, Beijing, PR China. [5]National Synchrotron Radiation Research Center, Hsinchu, Taiwan. [6]Department of Applied Physics, The Hong Kong Polytechnic University, Hong Kong, PR China. [7]Department of Physics, National Tsing Hua University, Hsinchu, Taiwan. [8]Department of Physics, University of Warwick, Coventry, UK. [9]These authors contributed equally: Zhibo Yao, Hao Cheng, Yifei Xu. ✉e-mail: xinyitan@bit.edu.cn; kevin.m.yang@polyu.edu.hk; sunzy@mail.buct.edu.cn

Atomically dispersed Ni–N_x sites are known to effectively catalyze the formation of CO via the ECR with a high atom utilization efficiency but suffer from the initial, intrinsically slow, PCET process[27–33]. In order to address this limit, we set out to introduce a second metal (M) atom next to the Ni–N_x to form a hetero-diatomic pair[34,35], with the selected M possessing a higher H adsorption property than Ni. This pair arrangement would enable facile generation of *H on the M site followed by its rapid migration to the CO_2 activated on the neighboring Ni site, thus synergistically facilitating the formation of *COOH and, in turn, faster ECR.

With this in mind, here we construct Ni-partnered heteronuclear diatomic catalysts (HDACs) with distinct H adsorption affinities, and apply them for high-efficiency and stable ECR. The as-developed HDACs exhibit extraordinary catalytic activity and selectivity, significantly outperforming the single-atom counterparts and many prior reported single-atom electrocatalysts. Based on combined theoretical and experimental investigations, we propose a hydrogen radical (H•) transfer-facilitated chemical hydrogenation mechanism. This unreported route is in contrast with the conventional first PCET pathway that suffers from a high required energy input, leading to greatly improved ECR performance for our HDAC. We also find that adjusting the H adsorption strength of the M site by selecting the element (i.e., Cd, Pt, and Pd) enables tuning of H• formation and simultaneously inhibits the hydrogen evolution side reaction, allowing for the CO_2 reduction rate to be optimized. A CO faradaic efficiency (FE_{CO}) reaching up to ~97.1% at ~ − 0.75 V versus reversible hydrogen electrode (vs. RHE) was attained and was able to maintain good stability even after 55.0 h of continuous CO_2 electrolysis. The FE_{CO} surpasses 90.0% within a broad range of current densities (*J*); from − 200.0 to − 600.0 mA cm^{-2}.

Results

Theoretical calculation of NiM−HDAC for CO_2 reduction

Density functional theory (DFT) calculations were first carried out using NiM−HDAC (M = Cd, Pt, or Pd) as a diatomic catalytic model. Various $NiMN_x$ configurations (Supplementary Figs. 1–3 and Table 1, and model information in Supplementary Data 1) were constructed and simulated, which show that the $NiMN_6$ structures possess relatively low formation energies, demonstrating their thermodynamic stability. Relative to Ni, all the M sites are found to be more likely to dissociate H_2O into *H and OH^-, and H is preferably adsorbed on the M sites (Supplementary Figs. 4–6). The adsorption strength of *H at M sites follows the trend: Cd > Pt > Pd. Given that the first PCET ($CO_2 + H^+ + e^- \rightarrow$ *COOH) is the critical step to yield CO during the ECR, the energy change for the *COOH formation ($E_{*COOH} - E_{*H + CO2}$) was calculated. It can be seen from Fig. 1a that $E_{*COOH} - E_{*H + CO2}$ decreases with the increase of ΔG_{*H}. That is, upon reducing the *H adsorption strength of the M site (ΔG_{*H}), the energy barrier for the formation of *COOH at the Ni site is lowered. This indicates that the ECR can be regulated by modulating the adsorption strength of *H at the M site.

The conversion of CO_2 to CO was further studied using $NiCdN_6$ and related structures as model catalysts. As illustrated in the calculated Gibbs free energy diagrams (Fig. 1b and Supplementary Data 1), for all catalysts, the formation of *COOH from CO_2 to CO is the PDS. In contrast to CdN_4 and $NiCdN_6$ (Cd site), which have a positive Gibbs free energy change for the transformation of *COOH to *CO, NiN_4 and $NiCdN_6$ with *H (i.e., Ni is the site for CO_2 activation) display a negative Gibbs free energy change for the hydrogenation process. It is noteworthy that the incorporation of Cd results in an apparent reduction in ΔG_{*COOH} from 1.78 eV on NiN_4 to 1.40 eV on $NiCdN_6$ with *H. If Cd is assumed as the active site for CO_2 adsorption and reduction, both

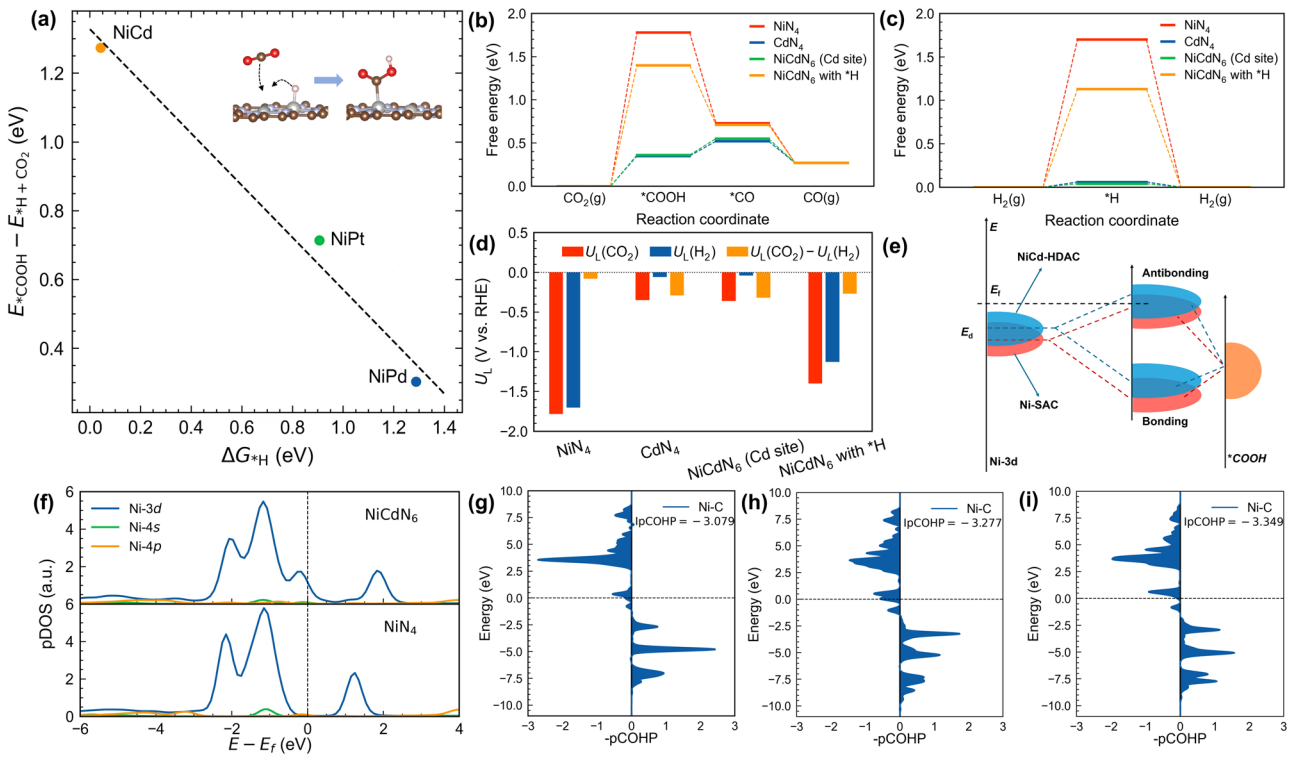

Fig. 1 | DFT calculations on the ECR reaction mechanism of NiM-HDAC catalysts. a Relationship between ΔG_{*H} and $E_{*COOH} - E_{*H + CO2}$ on NiM−HDAC catalysts, with the inset showing the schematic diagram of the cleavage of X−H bond to form *COOH. **b**, **c** Calculated Gibbs free energy diagrams for (**b**) the electroreduction of CO_2 to CO and (**c**) HER on the NiN_4, CdN_4, $NiCdN_6$ (Cd site), and $NiCdN_6$ with *H sites. **d** Calculated limiting potentials for CO_2 reduction, H_2 evolution, and their difference. **e** Schematic illustration explaining the change of metal-adsorbate interaction by altering the metal d band center. **f** pDOS of Ni in NiN_4 and $NiCdN_6$. pCOHP analysis of the Ni−C bond on (**g**) NiN_4, (**h**) $NiCdN_6$, and (**i**) $NiCdN_6$ with *H. Source data are provided as a Source Data file.

https://doi.org/10.1038/s41467-024-53529-2

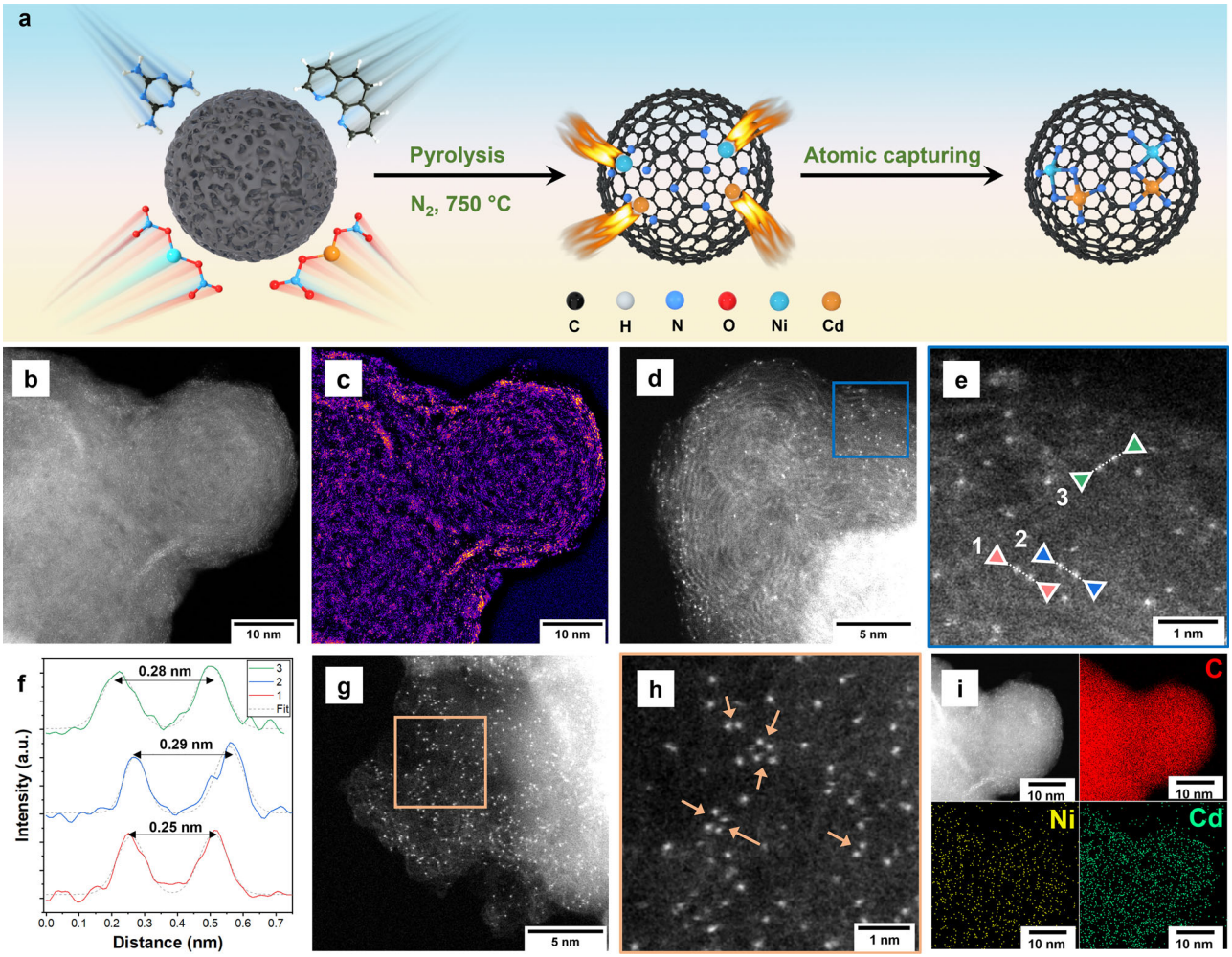

Fig. 2 | Synthesis and characterization of NiCd–HDAC. a Schematic illustration of the synthesis of NiCd–HDAC. **b** Low-magnification HAADF-STEM image of NiCd–HDAC. **c** Bandpass filtered false color lookup table of (**b**). **d** High-magnification HAADF-STEM image. **e** Detailed examination of a basal-plane region, from the highlighted region in (**d**). **f** Box averaged intensity profiles acquired across the indicated atom pairs in (**d**), with Gauss-fitted peaks. **g** High-magnification HAADF-STEM image and **h** enlarged image showing Ni and Cd atoms distributed on the support. **i** HAADF-STEM image and the corresponding EDS elemental maps of NiCd–HDAC.

CdN_4 and $NiCdN_6$ (Cd site) have the lowest energy barrier. However, the calculated Gibbs free energy profiles for the HER (Fig. 1c) show that the Cd sites in the two catalysts are more prone to producing *H rather than *COOH, with *H produced via the Cd-catalyzing Volmer reaction ($H_2O + e^- \rightarrow {}^*H + OH^-$ in neutral medium and $H_3O^+ + e^- \rightarrow {}^*H + H_2O$ in acidic catholyte). In addition, the second electron transfer to form a *CO intermediate for the two catalysts demands a high energy input, in stark contrast to the spontaneous process occurring on $NiCdN_6$ with *H. Therefore, we propose that $NiCdN_6$ with *H instead of $NiCdN_6$ (Cd site) is the most likely reaction model. Specifically, Ni serves as the active center for ECR, and Cd is the main site for the generation of *H. With the reaction model determined, the catalytic selectivity was then estimated by calculating the difference between the thermodynamic limit potential of CO_2 reduction and H_2 formation (denoted as U_L (CO_2) − U_L (H_2)). The larger (less negative) the value, the higher the ECR selectivity. Based on this metric, $NiCdN_6$ with *H outperforms both CdN_4 and $NiCdN_6$ (Cd site) (Fig. 1d), suggesting its superior ECR selectivity. Although NiN_4 gives better selectivity for CO_2 reduction over H_2 evolution compared to the other three catalysts, it presents a higher barrier for *COOH formation, thus hindering the overall reaction rate.

We calculated the projected density of states (pDOS) of the *d*-orbitals of the catalysts. It can be observed that the introduction of Cd leads to an upshift of the d band of Ni from − 2.24 to − 2.08 eV, driving further antibonding electronic levels over the E_f. This is conducive to supporting CO_2 adsorption and improving the binding affinity of intermediates on the $NiCdN_6$ site (Fig. 1e, f and Supplementary Data 1). Projected crystal orbital Hamilton population (pCOHP) analysis was also conducted to study the bonding–antibonding properties of the metal–adsorbate bond. As depicted in Fig. 1g–i and Supplementary Data 1, the negative pCOHP (right) represents the bonding contribution, and the positive pCOHP (left) stands for the antibonding contribution. The adsorption of *COOH is mainly attributed to the hybridization of Ni 3*d* orbitals and C 2*p* orbitals. The incorporation of Cd alters the 3*d* orbitals of Ni, and thus profoundly affects the binding strength of Ni and *COOH. The strengthened Ni–C interaction is verified by a more negative integrated COHP (IpCOHP) value of − 3.349 eV on $NiCdN_6$ with *H, compared to that of − 3.079 eV on NiN_4 and − 3.277 eV on $NiCdN_6$.

Synthesis and structural characterization of NiCd–HDAC

With these insights provided by first-principles calculations, the NiCd–HDAC atomic pair was then prepared via a facile combined complexation and pyrolysis method based on a strategy of heteroatom trapping. As illustrated in Figs. 2a, 1, 10 phenanthroline was first complexed with a mixture of nickel acetate and cadmium nitrate.

The resulting metal complex was subsequently adsorbed on acid-treated carbon black mixed with melamine, which was then subjected to calcination at 750.0 °C under an N_2 atmosphere. The melamine decomposed during the pyrolysis process, providing sufficient N species to dope the carbon support and also coordinate with Ni and Cd. Single-atom catalyst (SAC) control samples with pure single metal dopants, including Ni–SAC and Cd–SAC, were fabricated using the same method but without the addition of cadmium nitrate or nickel acetate, as appropriate. The X-ray diffraction (XRD) patterns of the three catalysts all display a strong peak at ~ 24.0° and a weak peak at ~ 44.0° arising from the characteristic (002) and (101) diffractions of graphitic carbon (Supplementary Fig. 7)[36]. No reflections originating from metal or metal compounds were found, suggesting the metal is well-dispersed as atoms and has not undergone nanoparticle nucleation.

The content of Cd was observed to increase concomitantly with the Ni amount, which suggests that the Ni–N structure captured and stabilized Cd to form NiCd–HDAC, thereby alleviating the vaporization of Cd (Supplementary Table 2). To understand this phenomenon, we performed DFT calculations. The results revealed that the formation energy of $NiCdN_6$ is lower than that of CdN_4 (Supplementary Table 3). This suggests that the presence of Ni favors the formation of $NiCdN_6$, which occurs more easily than the formation of CdN_4 in the absence of Ni. That is, Cd atoms can be trapped by Ni to form diatomic sites.

To further unravel the microstructure and dispersion of NiCd–HDAC, high-angle annular dark-field scanning transmission electron microscopy (HAADF-STEM) was performed. STEM images clearly show a high density of bright dots homogeneously dispersed on the surface of the NC support. These can be ascribed to Ni and Cd objects due to the atomic number contrast of HAADF-STEM, with the heavy metal atoms appearing brighter than either the C and N of the support (Fig. 2b–d). No nanoparticles, aggregates, or agglomerates of Ni and Cd were identified. Figure 2c shows a bandpass filter of Fig. 2b, with a false-color lookup table indicating the absence of nanoparticle formation. Imaging the sample at high magnification reveals that many of the single atoms form into atomic pairs, with a measured average distance of ~ 0.27 nm between pairs (Fig. 2e–h), implying the possible formation of heteronuclear atoms via metal–metal (Ni–Cd) bonds and the strong electronic perturbation between the two atoms. The presence of Ni and Cd species was also confirmed by inductively coupled plasma atomic emission spectroscopy (ICP-AES, Supplementary Table 2) and energy-dispersive X-ray spectroscopy (EDS) elemental maps (Fig. 2i).

The Raman spectrum of NiCd–HDAC (Supplementary Fig. 8) reveals signals at ~ 1338.0 and ~ 1595.0 cm^{-1}, which can be attributed to disordered sp^3 carbon (D band) and graphitic sp^2 carbon (G band), respectively. NiCd–HDAC possessed a higher peak intensity ratio between the D and G band (I_D/I_G) compared to Ni–SAC and Cd–SAC, indicating its more prevalent carbon defects. The surface composition and chemical states of the catalysts were probed by X-ray photoelectron spectroscopy (XPS), with the N 1*s* spectrum exhibiting three main peaks at ~ 397.9, 399.1, and 400.6 eV, corresponding to pyridinic N, pyrrolic N, and graphitic N, respectively[37]. The fraction of pyridinic N in all nitrogen configurations is ~ 11.3, 18.4, and 32.8% for Ni–SAC, Cd–SAC, and NiCd–HDAC, respectively. This may be associated with the higher content of NiCd–HDAC and the possible coordination of metal with pyridinic N (Supplementary Fig. 9a). No Ni^0 and Cd^0 XPS peaks are discernible, confirming that the metal atoms are predominantly coordinated with N instead of forming nanoparticles or clusters. A down-shift in the Ni signal (872.9 eV) is observed for NiCd–HDAC relative to that of Ni–SAC (873.1 eV). This contrasts with the Cd peak (412.4 eV), which is up-shifted as compared to that of Cd–SAC (412.3 eV) (Supplementary Fig. 9b, c), indicating the higher oxidation state of Cd in the NiCd–HDAC. The analysis of charge density difference shows that the oxidation state of Ni in NiCd–HDAC is lower than that in Ni–SAC, while the oxidation state of Cd is higher in the partnered atoms than that of the single Cd–SAC (Supplementary Fig. 10 and Table 4), in good agreement with the XPS results.

Synchrotron radiation X-ray absorption fine structure (XAFS) measurements were carried out to further investigate the electronic states and atomic configurations of Ni and Cd in the as-obtained materials. Figure 3a presents the X-ray absorption near-edge structure (XANES) spectra at the Ni K-edge for NiCd–HDAC and Ni–SAC as well as for commercial Ni foil and NiO. The absorption edge position of both NiCd–HDAC and Ni–SAC is located between those of Ni foil and NiO, implying that the average oxidation state of Ni is between 0 and + 2, with the oxidation state of Ni in NiCd–HDAC lower than that of Ni–SAC. Figure 3b provides the Cd K-edge XANES spectra of NiCd–HDAC and Cd–SAC. It shows that the absorption edge is also between those of Cd foil and CdO, further suggesting that the average oxidation state of Cd is between 0 and + 2. The oxidation state of Cd in NiCd–HDAC is slightly higher than that of Cd–SAC. These observations are consistent with the above-mentioned XPS results, signifying the strong Ni–Cd coupling interaction.

The bonding structure of Ni was examined by Fourier-transform fitting of the k^3-weighted extended X-ray absorption fine structure (EXAFS) spectra of Ni K-edges (Fig. 3c and Supplementary Table 5). Both NiCd–HDAC and Ni–SAC show a major peak at 1.87 Å, resulting from the Ni–N first shell coordination. The metal Ni–Ni bond at 2.48 Å is completely absent for both catalysts, further verifying the atomic dispersion of the metal species. Notably, a new scattering path at about 2.63 Å can be observed in the spectrum of NiCd–HDAC, which is neither from Ni–N (1.87 Å) nor from metallic Ni–Ni (2.48 Å). In the Cd K-edge FT-EXAFS spectra (Fig. 3d and Supplementary Table 6), a dominant peak at 2.27 Å is resolved for Cd–N first shell coordination.

For interpreting these results, it is important to consider that distinguishing between metal–N and metal–O coordination is difficult due to their similar peak positions in the EXAFS spectrum. A recent study showed that O coordination with the metal is supplanted by N with increasing temperature since O evaporates more readily than N[38]. Given that our work uses similar metal precursors containing O and a comparable pyrolysis temperature to this study, we speculate that the metal M in our samples is more likely to coordinate with N rather than O. To further substantiate this hypothesis, we conducted extensive DFT calculations and scrutinized all plausible configurations of $NiMON_5$ (M = Cd, Pd, Pt) (Model information in Supplementary Data 1) and compared their formation energy to that of $NiMN_6$ structures, considering the chemical potentials of oxygen and nitrogen (Supplementary Figs. 11, 12). It was found that only within a limited parameter space does $NiMON_5$ exhibit marginally lower formation energies than $NiMN_6$. Outside this range, the system favors the $NiMN_6$ configuration. Taking into account our experimental conditions, reference reports, and DFT calculations, we suggest that the prominent peak at approximately 1.5 Å in the EXAFS spectrum mainly reflects M–N, rather than M–O coordination.

A minor path at 2.62 Å is also discerned in the spectrum of NiCd–HDAC at the Cd K-edge, similar to the one observed in the Ni K-edge. This path can be reasonably explained as a Ni–Cd interaction contribution according to quantitative least-squares EXAFS fitting analysis (Fig. 3e, f), and the bond length matches the distance between the two atoms measured in the STEM images (Fig. 2e, f). At the same time, quantitative least squares EXAFS curve fitting was performed on DFT models of NiNi–DAC and CdCd–DAC. The results showed that they could not be well fitted, thus excluding the formation of homonuclear atom pairs (Supplementary Figs. 13, 14). Wavelet transformed (WT)-EXAFS was also conducted to investigate the adjacent properties of metal atoms. We compared the experimental results with the DFT model for the wavelet transform, and the two match almost perfectly, which confirms the accuracy of the NiCd–HDAC model (Fig. 3g). To further explore the overlapping contributions of different types of

https://doi.org/10.1038/s41467-024-53529-2

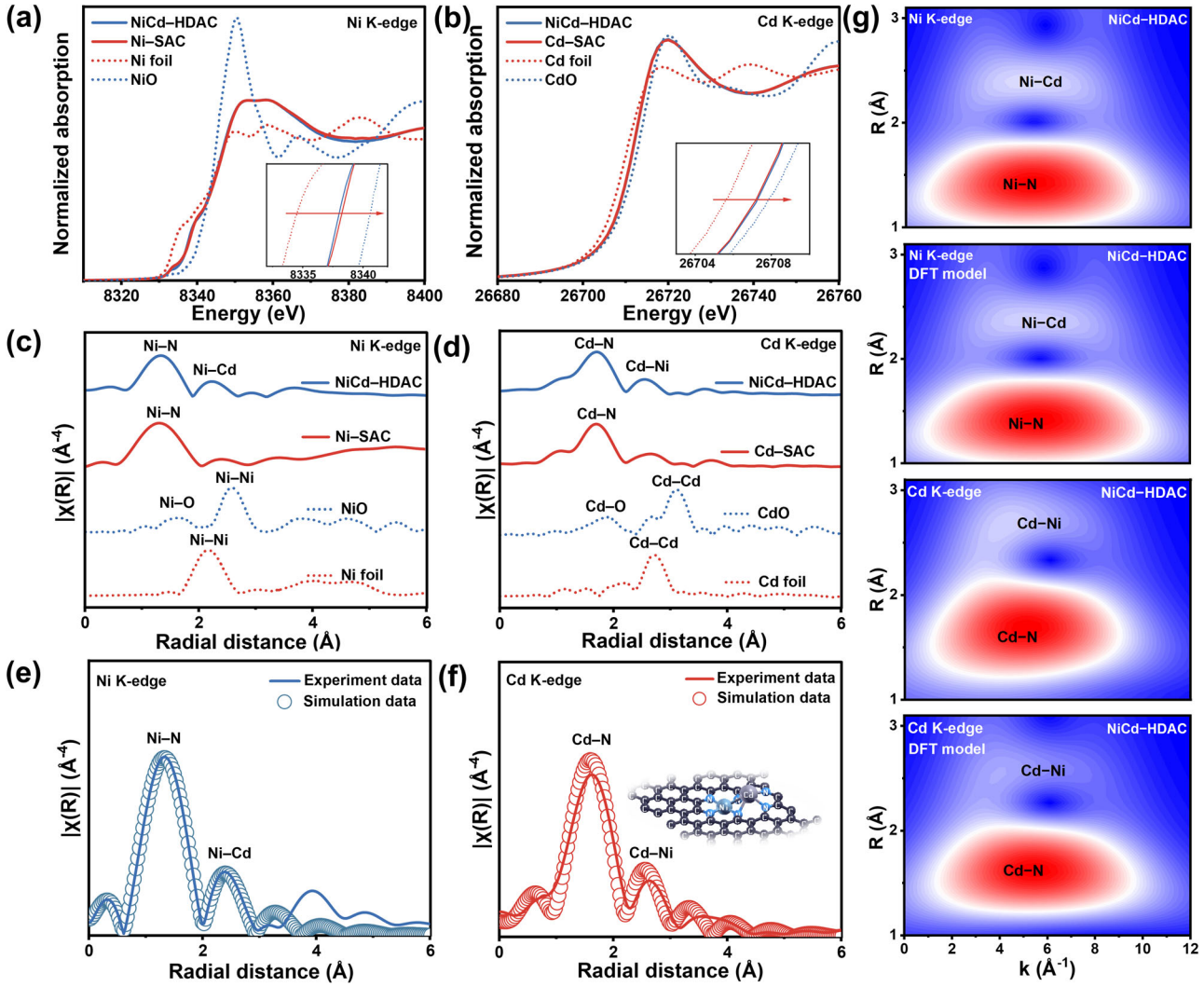

Fig. 3 | Spectral characterization of NiCd–HDAC. a Ni K-edge XANES spectra of NiCd–HDAC, Ni–SAC, and Ni reference materials. The inset shows the enlarged region of the absorption edge. **b** Cd K-edge XANES spectra of NiCd–HDAC, Cd–SAC, and Cd reference materials. The inset shows the enlarged region of the absorption edge. **c** Ni K-edge Fourier-transformed (FT) EXAFS spectra of NiCd–HDAC, Ni–SAC, and Ni reference materials. **d** Cd K-edge FT-EXAFS spectra of NiCd–HDAC, Cd–SAC, and Cd reference materials. **e** Experimental and fitting Ni K-edge EXAFS spectra of NiCd–HDAC. **f** Experimental and fitting Cd K-edge EXAFS spectra of NiCd–HDAC. **g** Ni K-edge and Cd K-edge WT-EXAFS spectra of NiCd–HDAC and DFT model of NiCd–HDAC. Source data are provided as a Source Data file.

atomic neighbors, the wavelet transform of the DFT model is disassembled. NiCd–HDAC shows an intensity maximum of 4.8 Å^{-1} for the Ni–N path at the Ni K-edge and an intensity maximum of 4.7 Å^{-1} for the Cd–N path at the Cd K-edge. For NiCd–HDAC, both WT signals derived from the Ni–metal bond and Cd–metal bond appear at ~ 6.3 Å^{-1}, suggesting the formation of a Ni–Cd bond. The WT signals at Ni and Cd K-edges are in accord with the FT-EXAFS results, corroborating the existence of metal–N coordination and Ni–Cd bonds in NiCd–HDAC.

Electrocatalytic CO_2-to-CO activity evaluation

The electrocatalytic properties of Ni–SAC, Cd–SAC, and NiCd–HDAC on ECR were studied using a home-made three-electrode H-cell with 0.1 M $KHCO_3$ solution as the catholyte and 0.1 M H_2SO_4 as the anolyte. The solution internal resistances of all catalytic systems were measured (Supplementary Table 7), and *iR* compensation (where *i* is a measured current and *R* is uncompensated resistance between the working and reference electrodes) was performed for all potentials. As revealed by linear sweep voltammetry (LSV) in Fig. 4a and Supplementary Fig. 15a, a substantially smaller current density was attained in Ar than in the CO_2 atmosphere, indicating the occurrence of CO_2 reduction on NiCd–HDAC. NiCd–HDAC exhibits a markedly higher cathodic reduction current than Ni–SAC and Cd–SAC, reflecting its superior electrocatalytic activity. The gas and liquid products were detected by gas chromatography (GC) and nuclear magnetic resonance (NMR) measurements, respectively (Supplementary Fig. 16). NiCd–HDAC outperforms Ni–SAC and Cd–SAC across the entire potential window from ~ − 0.50 to − 0.99 V (vs. RHE) in terms of FE toward CO, reaching an FE_{CO} maximum of ~ 97.1 ± 0.2% at − 0.75 V (vs. RHE). The FE_{CO} is greater than 90.0% within a wide potential range from ~ − 0.59 to − 0.91 V (vs. RHE) on NiCd–HDAC (Fig. 4b and Supplementary Table 8). Likewise, NiCd–HDAC exhibits apparently larger CO partial current density (J_{CO}) than the single atom counterparts throughout the applied voltage range from ~ − 0.50 to − 0.99 V (vs. RHE) (Supplementary Fig. 17a). For the sake of comparison, physically mixed Ni–SAC and Cd–SAC (mix-Ni,Cd–SAC) was also tested for the ECR (Supplementary Fig. 17b, c and Supplementary Table 9), which demonstrated both lower J_{CO} and FE_{CO} compared to NiCd–HDAC, demonstrating the advantage of hetero-diatomic sites in NiCd–HDAC.

The Cd content can be adjusted by tuning the Ni content, as discussed earlier in the manuscript. Compared to Cd–SAC, the content of Cd in NiCd–HDAC was found to be higher (Supplementary Table 2). Upon improving the Ni content from 0.49 to 0.86 wt%, the content of

https://doi.org/10.1038/s41467-024-53529-2

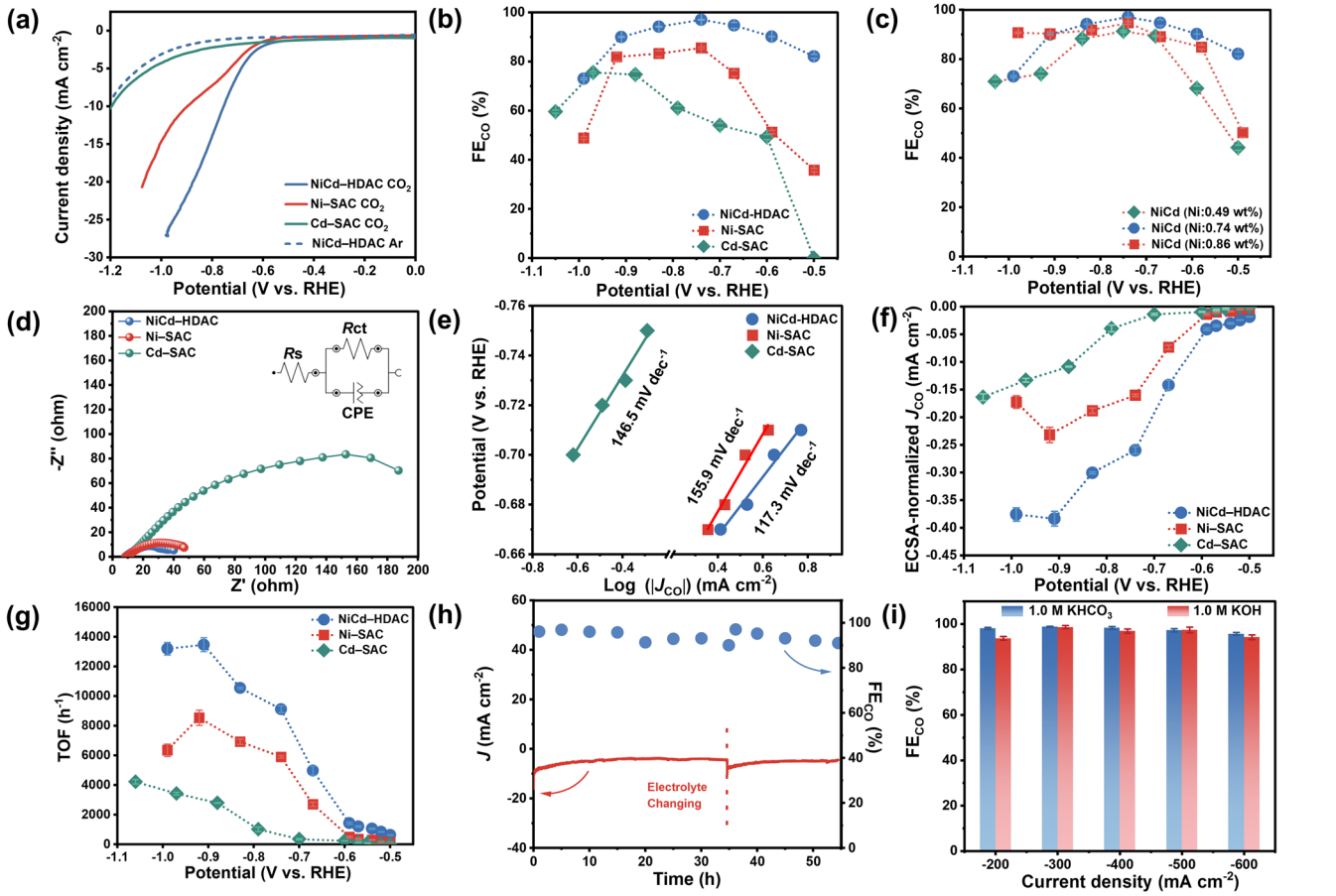

Fig. 4 | ECR performance. a LSV curves of Ni–SAC, Cd–SAC, and NiCd–HDAC acquired on a rotating disc electrode at 500.0 rpm with a scan rate of 5.0 mV s^{-1} in Ar- or CO_2-saturated 0.1 M $KHCO_3$ solution. **b** CO FE against applied potential. **c** CO FE of NiCd–HDAC with different Ni contents. **d** Nyquist profiles, (**e**) Tafel plots for CO production, (**f**) electrochemical active surface area (ECSA)-normalized CO partial current densities, and (**g**) TOFs of Ni–SAC, Cd–SAC, and NiCd–HDAC. The inset in (**d**) illustrates the equivalent circuit used for fitting the data, where R_S shows the combination of the resistance of electrodes and electrolyte, and CPE and *R*ct represent the capacitance and charge transfer resistance of the working electrode-electrolyte interface, respectively. **h** Current–time response and the corresponding CO FE on NiCd–HDAC at a fixed potential of ~ − 0.75 V (vs. RHE). **i** CO FE as a function of cathodic current density on NiCd–HDAC in 1.0 M KOH or $KHCO_3$ catholyte operated in a flow cell. For panels (**a**, **b**, **c**, **e**, **f**, **g**, and **h**), *iR* correction was applied. The average *R* with a standard error (SE) from three independent measurements for Ni-SAC, Cd-SAC, and NiCd-HDAC is 8.76 ± 0.05 Ω, 9.89 ± 0.13 Ω, and 8.69 ± 0.02 Ω, respectively. Data in (**b**, **c**, **f**, **g**, and **i**) are represented as mean ± SE from two independent measurements. Source data are provided as a Source Data file.

Cd in NiCd–HDAC was observed to increase from 1.52 to 2.13 wt%. The ECR activity of NiCd–HDAC was tunable by tailoring the Ni content, with 0.74 wt% affording the highest FE_{CO} (Fig. 4c and Supplementary Table 10). Further, an increase in Ni content led to a slight decrease in FE_{CO} for the potentials ranging from ~ − 0.5 to − 0.93 V (vs. RHE), which was probably due to the concurrent increase of Cd content and thus increased HER. Whereas for more negative potentials beyond − 0.93 V (vs. RHE), the FE_{CO} increased with Ni content, likely owing to the slower diffusion kinetics of dissolved CO_2 molecules and, therefore, more accessible Ni sites thwarting the parasitic HER. As seen in Supplementary Fig. 17d, J_{CO} increased with the increase of Ni content over the entire potential range, which is associated with more Ni–Cd bimetallic sites forming and thus enhanced reaction kinetics. When the Ni content was further improved beyond 0.86 wt%, a pronounced drop in both FE_{CO} and J_{CO} was observed (Supplementary Fig. 18 and Supplementary Table 11). This may be associated with the further increase in Cd content and the appearance of Ni clusters, which resulted in more intense HER.

Electrochemical impedance spectroscopy (EIS) Nyquist plots (Fig. 4d) indicate that NiCd–HDAC possesses a significantly lower interfacial charge-transfer resistance (R_{CT}) than Ni–SAC and Cd–SAC, thus providing the highest electron transfer efficiency during the ECR. Moreover, NiCd–HDAC displays the lowest Tafel slope (117.3 mV dec^{-1}) as compared with Ni–SAC (155.9 mV dec^{-1}) and Cd–SAC (146.5 mV dec^{-1}) (Fig. 4e). This suggests that the NiCd–HDAC greatly accelerates the CO_2-CO conversion kinetics. The partial geometry current densities toward CO formation were normalized based on electrochemical active surface area (ECSA). ECSA is estimated based on the Helmholtz double layer capacitance (C_{dl}) by ECSA = C_{dl}/C_s (Supplementary Figs. 19 and 20a), where C_s is the average specific capacitance (0.04 mF cm^{-2}). It is noted that NiCd–HDAC possesses markedly higher values of ECSA-normalized J_{CO} than both Ni–SAC and Cd–SAC across the potential range from ~ − 0.50 to − 0.99 V (vs. RHE), indicating its superior intrinsic activity (Fig. 4f). In addition, within the potential window, the turnover frequency (TOF) values of NiCd–HDAC are much higher than those of Ni–SAC and Cd–SAC (Fig. 4g). Beyond that, NiCd–HDAC manifests good catalytic stability with minimal decay in current and nearly constant FE_{CO} even after 55.0 h of continuous electrolysis (Fig. 4h). Post-reaction characterization by HAADF-STEM along with EDS showed that the uniform distribution of diatomic NiCd–HDACs was maintained after electrolysis (Supplementary Fig. 21).

To circumvent the mass transfer limitation of CO_2 in an H-type electrolytic reactor, a flow cell with a gas diffusion electrode (GDE) was designed and implemented in order to evaluate the potential of the NiCd–HDAC for industrial applications. A FE_{CO} over 90.0% within a broad current density range from − 200.0 to − 600.0 mA cm^{-2} was

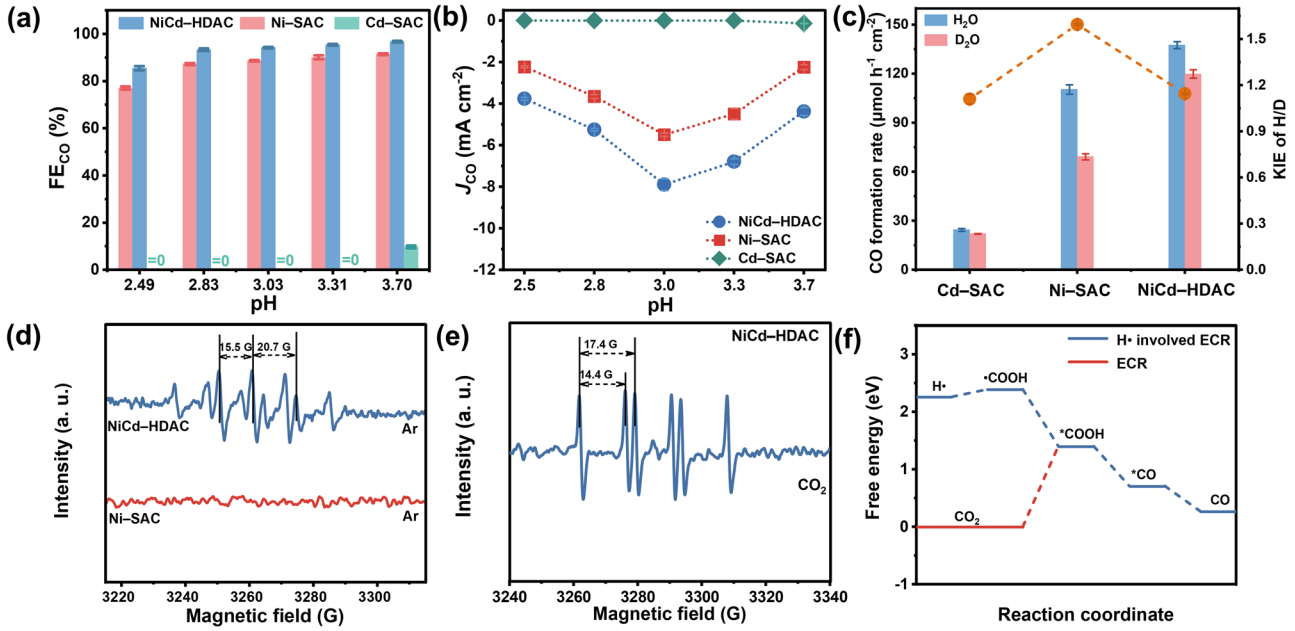

Fig. 5 | The mechanism of hydrogen radical facilitated ECR reaction. a CO FEs and (**b**) CO partial geometric current densities for Ni–SAC, Cd–SAC, and NiCd–HDAC in electrolytes with different pH values (by adding 0.1 M H_2SO_4 to 0.1 M KCl to adjust pH, and the pH values with SEs were 2.49 ± 0.02, 2.83 ± 0.02, 3.03 ± 0.01, 3.31 ± 0.04, 3.70 ± 0.04, respectively) at ~ − 0.8 V (vs. RHE). **c** CO formation rates (column) and KIE values (ball) of Ni–SAC, Cd–SAC, and NiCd–HDAC. For panels (**a**, **b**, and **c**), *iR* correction was applied. The average *R* with an SE from three independent measurements was shown in Supplementary Table 15. Data in (**a**, **b**, and **c**) are represented as mean ± SE from two independent measurements. **d** Operando EPR spectra of the solutions obtained after 6.0 min of ECR in 0.1 M $KHCO_3$ under Ar using DMPO as an •H-trapping reagent on Ni–SAC and NiCd–HDAC. **e** Operando EPR spectra of the solutions obtained after 6.0 min of ECR in 0.1 M $KHCO_3$ under CO_2 using DMPO as an •H-trapping reagent on NiCd–HDAC. **f** Free-energy diagrams of ECR on $NiCdN_6$ with *H. Source data are provided as a Source Data file.

attained on NiCd–HDAC in both 1.0 M $KHCO_3$ and KOH solutions (Fig. 4i and Supplementary Table 12). In particular, the FE_{CO} and J_{CO} reach as high as ~ 95.7% and − 574.3 mA cm^{-2}, respectively, superior to many recently reported electrocatalysts (Supplementary Table 13). We also found that NiCd–HDAC's performance still significantly exceeds Ni–SAC and Cd–SAC, in terms of both FE_{CO} and J_{CO} (Supplementary Fig. 20b–d and Supplementary Table 14), when used in a flow electrolytic cell, consistent with the aforementioned H-cell results. 1.0 M $KHCO_3$ outperforms 1.0 M KOH in terms of FE_{CO} over the current range, which may be due to the higher local concentration of hydrogen radicals available in the former catholyte. $KHCO_3$ solution is also preferred due to being less susceptible to salt deposition at the cathode over extended operation.

Investigation of CO_2-to-CO reaction mechanism

To gain insight into the reaction mechanism on the catalyst surface, the proton concentration of the catholyte was adjusted by the controlled addition of 0.1 M H_2SO_4 solution. At pH ≤ 3.3, no ECR reaction takes place on Cd–SAC (Fig. 5a and Supplementary Table 15). Instead, HER exclusively occurs on Cd–SAC under this acidic pH due to its propensity for favoring the water splitting reaction (i.e., due to the preferred adsorption of H^+ on Cd sites) rather than the CO_2 reduction reaction, consistent with the DFT results. At these low pH values, surprisingly, NiCd–HDAC still maintains a high CO FE of 90.0%, even down to a low pH of 2.8. Interestingly, with the increase of proton concentration, J_{CO} does not monotonously drop, but rises first and then decreases, showing a volcano profile (Fig. 5b). During the ECR, the yield and concentration of *H profoundly affect the reaction rate. Upon decreasing the pH from 3.7 to 3.0, the reduction rate of CO_2 on both NiCd–HDAC and Ni–SAC is enhanced, which arises from the continuous generation and rapid consumption of *H at this pH range. However, further increasing the proton concentration leads to a drop in the CO_2 reduction rate, which is likely due to fewer dissolved CO_2 molecules. Note that NiCd–HDAC has a strikingly higher FE and J_{CO} than Ni–SAC in different pH solutions. This can be attributed to two properties; first, the *H generated at the Cd site promotes proton transfer to enhance the ECR; and second, the introduction of Cd improves the d band center of Ni and thereby accelerates electron transfer.

To understand the role of Cd in boosting protonation during the ECR, we investigated the kinetic isotope effect (KIE) of H/D (H_2O/D_2O) over Ni–SAC, Cd–SAC, and NiCd–HDAC (Fig. 5c). The KIE can be used as an indicator of proton transfer rate during water dissociation, which can therefore provide information on the ECR protonation kinetics. The KIE of NiCd–HDAC is determined to be 1.15, substantially lower than that of Ni–SAC (1.60). This implies that the Cd sites in NiCd–HDAC enhance the dissociation of water and largely promote proton transfer during the ECR. The KIE of Cd–SAC was calculated to be 1.11, signifying that the water splitting on Cd sites is relatively fast, and can supply sufficient *H for CO_2 hydrogenation. The main factor limiting ECR on Cd–SAC is the competitive adsorption of CO_2 and H^+, rather than the further hydrogenation after CO_2 adsorption. Taken together, we infer that the Ni sites in NiCd–HDAC mainly adsorb CO_2, while the Cd sites catalyze the Volmer reaction to yield *H, synergistically enhancing the CO_2-to-CO conversion.

Interestingly, we discovered that Cd helps to generate H•, which was validated by operando electron paramagnetic resonance (EPR) spectroscopy with 5,5-dimethyl-1-pyrrolidine-N-oxide (DMPO) as a radical-trapping reagent. Nine characteristic peaks with a corresponding peak intensity ratio of 1:1:2:1:2:1:2:1:1 are clearly observed for NiCd–HDAC under an Ar atmosphere at − 0.6 V (Fig. 5d), agreeing well with the simulation results, which are assigned to DMPO-•H (A_N = 20.7 G, A_H = 15.5 G)[39]. In contrast, no EPR signal was obtained for Ni–SAC (Fig. 5d), suggesting that the formation of H• in NiCd–HDAC is attributed to Cd. When CO_2 was introduced, the typical 9 signals disappeared, indicating that the produced H• is consumed by the

https://doi.org/10.1038/s41467-024-53529-2

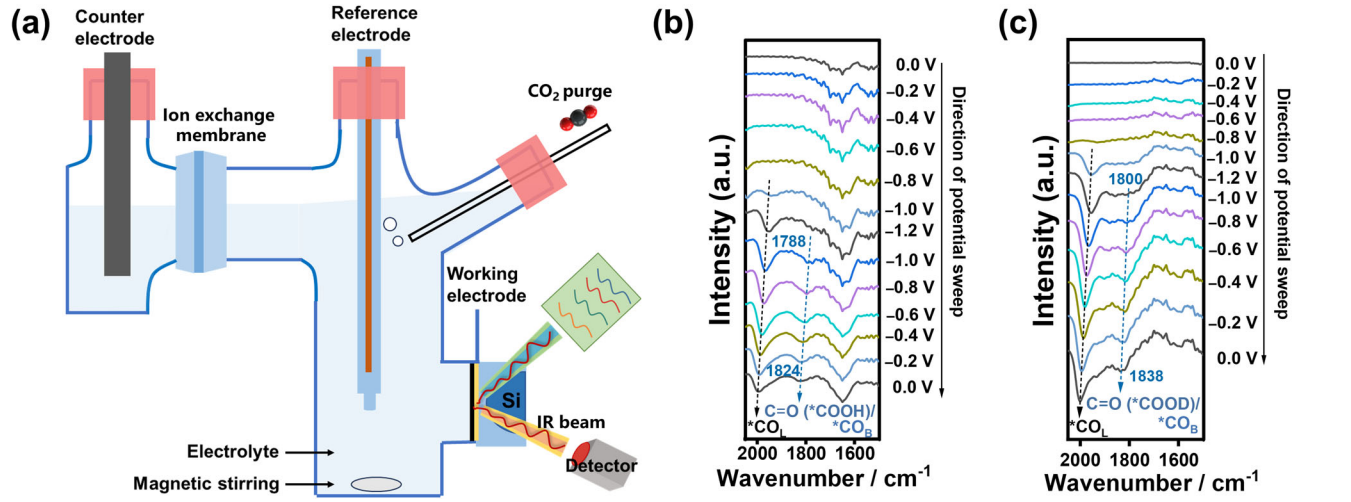

Fig. 6 | Electrochemical and operando ATR-SEIRAS analyses for the NiCd–HDAC. **a** Schematic illustration of operando ATR-SEIRAS tests. Operando ATR-SEIRAS spectra of NiCd–HDAC in (**b**) CO_2-saturated 0.1 M $KHCO_3$ dissolved in H_2O and (**c**) CO_2-saturated 0.1 M K_2CO_3 dissolved in D_2O at various applied voltages in the regions of 1700–2050 cm^{-1}. No *iR* correction was applied for panels (**b**) and (**c**). Source data are provided as a Source Data file.

intermediates in the ECR process. EPR has also been reported to be sensitive to detecting carboxyl radicals[39]. It is noted that the CO FE of the NiCd–HDAC catalyst is exceedingly high, leaving only trace amounts of •COOH remaining to be detected by EPR. Indeed, EPR signals for •COOH (A_N = 17.4 G, AH = 14.4 G) emerged (Fig. 5e)[40], indicating that the H• can effectively activate CO_2 to generate •COOH. These results strongly evidence the key role of H• radicals in CO_2 reduction. This proposed mechanism was further investigated by DFT calculations. As shown in Fig. 5f and Supplementary Data 1, NiCd–HDAC requires a particularly high free energy variation of about 1.4 eV to form *COOH through PCET. However, with the aid of H•, the first hydrogenation of CO_2 molecules was calculated to occur more easily ($\Delta G_{(H\bullet\rightarrow COOH)}$ = 0.13 eV). Thus, we propose that the ECR process undergoes a H• transfer pathway with a significantly decreased free-energy barrier. The first step is the activation of CO_2 by H•, giving rise to •COOH, followed by the exothermic •COOH adsorption (*COOH) on Ni. The overall reaction pathways can be summarized as follows:

$$H_2O + M + e^- \rightarrow M - H + OH^- \quad (1)$$

$$M - H \rightarrow M + H\cdot \quad (2)$$

$$H\cdot + CO_2 \rightarrow \cdot COOH \quad (3)$$

$$\cdot COOH + Ni \rightarrow Ni - COOH \quad (4)$$

$$Ni - COOH + H^+ + e^- \rightarrow Ni - CO + H_2O \quad (5)$$

$$Ni - CO \rightarrow CO + Ni \quad (6)$$

To examine possible reaction intermediates during the ECR, operando attenuated total reflection surface-enhanced infrared absorption spectroscopy (ATR-SEIRAS) measurements were performed (Fig. 6, and Supplementary Figs. 22 and 23). As displayed in Fig. 6b and Supplementary Fig. 22a, seven peaks at ~1230, 1330, 1460, 1650, 1788, 1967, and 3230 cm^{-1} were observed in CO_2-saturated $KHCO_3$ aqueous electrolytes at an applied potential of − 1.1 V (vs. RHE). The peak at ~1230 cm^{-1} is associated with Si–O, and comes from the exposed substrate on which the ATR-SEIRAS active film is deposited[41]. The signal at ~1330 cm^{-1} arises from the symmetric stretching vibration of bulk HCO_3^- in the electrolytes[41]. The ~3230 cm^{-1} region is assigned to the O–H stretching mode of H_2O. The distinct band at ~1967 cm^{-1} originates from linearly adsorbed *CO ($*CO_L$)[42,43], which showed Stark tuning when changing the potential (a blueshift by ~26 cm^{-1} with the variation of sweep potential from − 1.1 to 0 V). The peak at ~1788 cm^{-1} can be attributed to the C = O stretching vibration (of *COOH) and/or C≡O stretching vibration of bridge-bound CO ($*CO_B$)[43], which blue-shifted as a function of increasing (less negative) potential. However, it remains ambiguous whether $*CO_B$ and *COOH coexist in this region in Fig. 6b. To clarify this, we conducted control experiments[43] by first switching CO_2 to CO and then back to CO_2 atmosphere during operando ATR-SEIRAS measurements under electrolysis at − 0.9 V (vs. RHE) (Supplementary Fig. 23). It was found that when switching CO_2 to CO, the $*CO_L$ peak (at ~1975 cm^{-1}) gradually increased and blue-shifted due to the increasing coverage of *CO before approaching an equilibrium after several SEIRAS scans (Supplementary Fig. 23a)[43], while the peak at the low wavenumber range (from 1808 to 1814 cm^{-1}) decreased with time initially and then stabilized. This suggests that the lower wavenumber band is due to a combined contribution of both $*CO_B$ and *COOH. The initial drop in peak intensity is likely due to the *COOH species gradually being converted and desorbed, leaving the surface free for adsorption of $*CO_L$. When the CO atmosphere was switched back to a CO_2 environment, a decrease in $*CO_L$ at the high wavenumber range coupled with a redshift was seen (Supplementary Fig. 23b), which could be ascribed to the decreased dipole–dipole interaction associated with the reduction in $*CO_L$ coverage[43]. Conversely, the peak at the low wavenumber range increased, suggesting that CO_2 is first reduced to *COOH, which then accumulates on the surface, thereby enhancing the broadband on account of the equilibrium $*CO_B$ coverage before the switching. As a result, the formation of both *COOH and *CO ($*CO_L$ and $*CO_B$) intermediates can be deduced, although the deconvolution of the peak is difficult due to the shift of peak position with both composition and coverage of surface species[43].

The peak at ~1460 cm^{-1} in Supplementary Fig. 22a could result from either CO_3^{2-} [44] or *COOH intermediate (C–O stretching)[45]. However, as no Stark tuning was observed for this peak, we can conclude that this peak originates from CO_3^{2-} in the electrolytes[44] generated from the reaction of dissolved CO_2 molecules and OH^- ions. The band at ~1650 cm^{-1} is likely an overlap of the O–H bending mode of H_2O and the asymmetric stretching vibration of solution HCO_3^- [41,44]. In prior work, the C = O stretching band of *COOH was also reported to appear

at 1654 cm^{-1} under − 1.6 V (vs. Ag/AgCl) on Ag[45]. To obviate between the potential contribution of water and bicarbonate ions, and further clarify whether the peak at ~1650 cm^{-1} is also from *COOH, we measured the operando ATR-SEIRAS spectra of CO_2-saturated K_2CO_3 electrolytes dissolved in D_2O. The results showed the absence of any peak at this position (Supplementary Fig. 22b). Therefore, the band at ~1650 cm^{-1} exhibited in Supplementary Fig. 22a is unlikely to be from *COOH on NiCd-HDAC. The bands shown in Fig. 6c and Supplementary Fig. 22b at ~1958 and 1800 cm^{-1} (at − 1.2 V vs. RHE) can be assigned to $*CO_L$ moieties[42] and *COOD (C = O stretching vibration)/$*CO_B$, respectively[43]. Both peaks were observed to blue-shift during the sweep to less negative potentials (by ~45 cm^{-1} for $*CO_L$ and ~38 cm^{-1} for *COOD/$*CO_B$ with the sweep potential from − 1.2 to 0 V). We also calculated the wavenumbers for *COOD and *COOH on NiCd−HDAC by DFT simulation (Supplementary Fig. 22c and Supplementary Data 1). A small redshift (~2.6 cm^{-1}) for C = O stretching of *COOD (as opposed to *COOH) was observed due to the replacement of hydrogen atoms with deuterium, agreeing well with prior results reported in literature[46]. The calculated bands are consistent with the peaks observed in the SEIRAS spectra (Fig. 6b, c). The deviation in peak positions with the experiment may be due to the overlap of *COOH(D) and $*CO_B$ bands, making it difficult to identify the *COOH(D) peak. The overlap of *COOH(D) and $*CO_B$ peaks in Fig. 6b, c also makes it challenging to identify whether the shift occurred by *COOD as opposed to *COOH. The band at ~2600 cm^{-1} results from the stretching vibrations of O−D[44], while the bending mode of O−D overlaps with the Si−O peak at ~1200 cm^{-1} (Supplementary Fig. 22b)[41]. A peak at ~1460 cm^{-1} without Stark effect was also discerned, which can be well assigned to solution CO_3^{2-} (Supplementary Fig. 22b). For both operando SEIRAS measurements in H_2O and D_2O, during the backward (anodic) scan from − 1.2 to − 0.6 V, the overlapping *COOH(D)/$*CO_B$ and $*CO_L$ peaks increased, which is likely due to the formation rates for the intermediates being faster than their conversion and desorption rates at this potential range. While upon further scanning from − 0.6 to − 0 V, the bands for both overlapping *COOH(D)/$*CO_B$ and $*CO_L$ decreased (Supplementary Fig. 23c, d). This could result from the desorption of the intermediates (from the NiCd−HDAC surface) being faster than their generation and conversion. During the backward scan at more positive potentials (e.g., 0 V), the accumulated peaks for *COOH(D) and *CO species did not disappear. This may be due to their more favorable adsorption on the surface of NiCd−HDAC as the potential becomes more positive[47,48].

Based on the above operando ATR-SEIRAS and DFT results, we can evidence the formation of *COOH and $*CO_B$ (at ~1788 cm^{-1} under − 1.0 V vs. RHE)[43] and $*CO_L$ (at ~1967 cm^{-1} under − 1.0 V vs. RHE)[42] intermediates on the surface of NiCd−HDAC. This is consistent with the aforementioned calculated reaction paths.

To test if the ECR activity can be further improved by augmenting with dissolved CO_2 according to the above-proposed mechanism, we conducted ECR in an H-cell using an ionic liquid solution (0.5 M 1-butyl-3- methylimidazolium hexafluorophosphate solution in acetonitrile, [Bmim]PF_6/MeCN) as the catholyte (Supplementary Figs. 24 and 25 and Table 16). The remarkable dissolving ability of [Bmim]PF_6 for CO_2 and its application for ECR to reduce CO_2 activation barriers have been demonstrated in prior literature[49]. It was found that NiCd−HDAC surpassed Ni−SAC and Cd−SAC in terms of both CO FE and partial current density. In particular, the FE toward CO formation approaches almost 100.0% at ~ − 2.17 V (vs. Ag/Ag^+) and over 96.7% within a wide potential window from ~ − 1.95 to − 2.21 V (vs. Ag/Ag^+) on NiCd−HDAC (Supplementary Fig. 25b). Strikingly, NiCd−HDAC delivers a CO partial current density as high as ~129.6 mA cm^{-2} at ~ − 2.17 V (vs. Ag/Ag^+), which is 2.6 and 3.0 times that of Ni−SAC at ~ − 2.27 V (vs. Ag/Ag^+) and Cd−SAC at ~ − 2.28 V (vs. Ag/Ag^+), respectively (Supplementary Fig. 25c). The ECR performance of Cd−SAC is surprisingly comparable to that of Ni−SAC in 0.5 M [Bmim]PF_6/MeCN electrolyte. This may correlate with the dramatically increased local concentration of CO_2 and decreased local concentration of protons at the electrode/electrolyte interface, enabling adsorption and activation of CO_2 on the Cd−SAC rather than the adsorption of hydrogen. To check if the catalytic properties stem from the simple sum of individual Ni−SAC and Cd−SAC, physically mixed Ni−SAC and Cd−SAC (mix-Ni,Cd−SAC) with equivalent metal loadings were examined for ECR, which nonetheless displayed substantially lower CO partial current densities across the applied voltage window in 0.5 M [Bmim]PF_6/MeCN catholyte, as compared to NiCd−HDAC. This further confirms the advantage of heteronuclear atom pairs for ECR (Supplementary Figs. 25d and 26).

At the start of this work, NiPt and NiPd were calculated to possess lower energy barriers for *COOH formation and, thus, better CO_2-to-CO conversion efficiency than NiCd. To check if this is the case in reality, NiPt−HDAC and NiPd−HDAC were synthesized based on a similar strategy as used for NiCd−HDAC. XRD patterns, XPS spectra, HAADF-STEM images, EDS spectra, and elemental maps show the formation of atomically dispersed NiPt and NiPd on the carbon support (Supplementary Figs. 27–29). The atomic number sensitive contrast of HAADF-STEM clearly shows the heavier metal atomic sites distributed across the carbon support, with no agglomeration or nanoparticle formation evident. EDS spectra of the samples confirm the metals to be Ni and Pt or Pd, with the Cu signal originating from the supporting TEM grid (see "Methods"). Resembling NiCd−HDAC, both NiPt−HDAC and NiPd−HDAC exhibit prominently higher FE_{CO} and CO partial current densities than their corresponding single atom counterparts (Fig. 7 and Supplementary Table 17) over the voltage regions, with the exception of NiPt−HDAC at ~ − 0.89 V, which shows a lower FE_{CO} than Ni−SAC. This may be due to the resulting optimal hydrogen adsorption at this potential on NiPt−HDAC. A FE_{CO} of 93.4 and 96.0% was attained on NiPt−HDAC and NiPd−HDAC at ~ − 0.74 and − 0.72 V (vs. RHE), respectively. The FE toward H_2 on NiPt−HDAC is larger than that of NiPd−HDAC and NiCd−HDAC, probably due to the optimal hydrogen adsorption affinity of Pt. Despite the increased propensity for HER on NiPt−HDAC and NiPd−HDAC compared to NiCd−HDAC, both afford a higher CO partial current density than NiCd−HDAC (within the margin of error) throughout the potential range, as depicted in Fig. 7f. The ECR performance was tunable by adjusting the molar ratio of Ni-to-Pt or Pd. The Ni-to-Pt or Pd molar ratio of 1:1 was found to be better than the other ratios in terms of both FE_{CO} and J_{CO} (Supplementary Fig. 30 and Supplementary Table 18). When the molar ratio of Pt-to-Ni was increased to 2.0, the resulting NiPt−HDAC catalyst exhibited marginal ECR activity, which may be due to the formation of many Pt clusters and the induced severe HER. Likewise, the ECR activity also substantially decreased when the molar ratio of Pd-to-Ni was increased to 2.0.

To further verify the H• transfer pathway on the NiM−HDAC, we investigated the ECR by introducing *tert*-butyl alcohol (*t*-BuOH) into the electrolyte, which can quickly eliminate the generated H• (Supplementary Fig. 31 and Supplementary Table 19). It is worth noting that after adding *t*-BuOH, the FE_{CO}, and J_{CO} of NiPd−HDAC, NiPt−HDAC, and NiCd−HDAC systems markedly decreased, indicating an H• transfer pathway in the catalytic reaction process. Meanwhile, similar experiments were conducted using Ni−SAC as a reference sample, and the results showed that the addition of *t*-BuOH did not affect FE_{CO} and J_{CO}, suggesting the absence of a H• transfer pathway in the Ni−SAC system. Operando EPR results revealed the generation of H• in both NiPt−HDAC and NiPd−HDAC, pointing to a H• transfer pathway akin to NiCd−HDAC. In addition, the DMPO-•H signal is strongest in NiPd−HDAC, moderate for NiPt−HDAC, and weakest in NiCd−HDAC (Supplementary Fig. 32). This is in close association with the weaker hydrogen adsorption strength of Pd relative to Pt and Cd, and in good agreement with the aforementioned DFT calculation results. The formed *H readily detaches from Pd's surface to form H• and then reacts with dissolved CO_2 molecules to generate •COOH, which is adsorbed on the surface of Ni to convert into CO.

https://doi.org/10.1038/s41467-024-53529-2

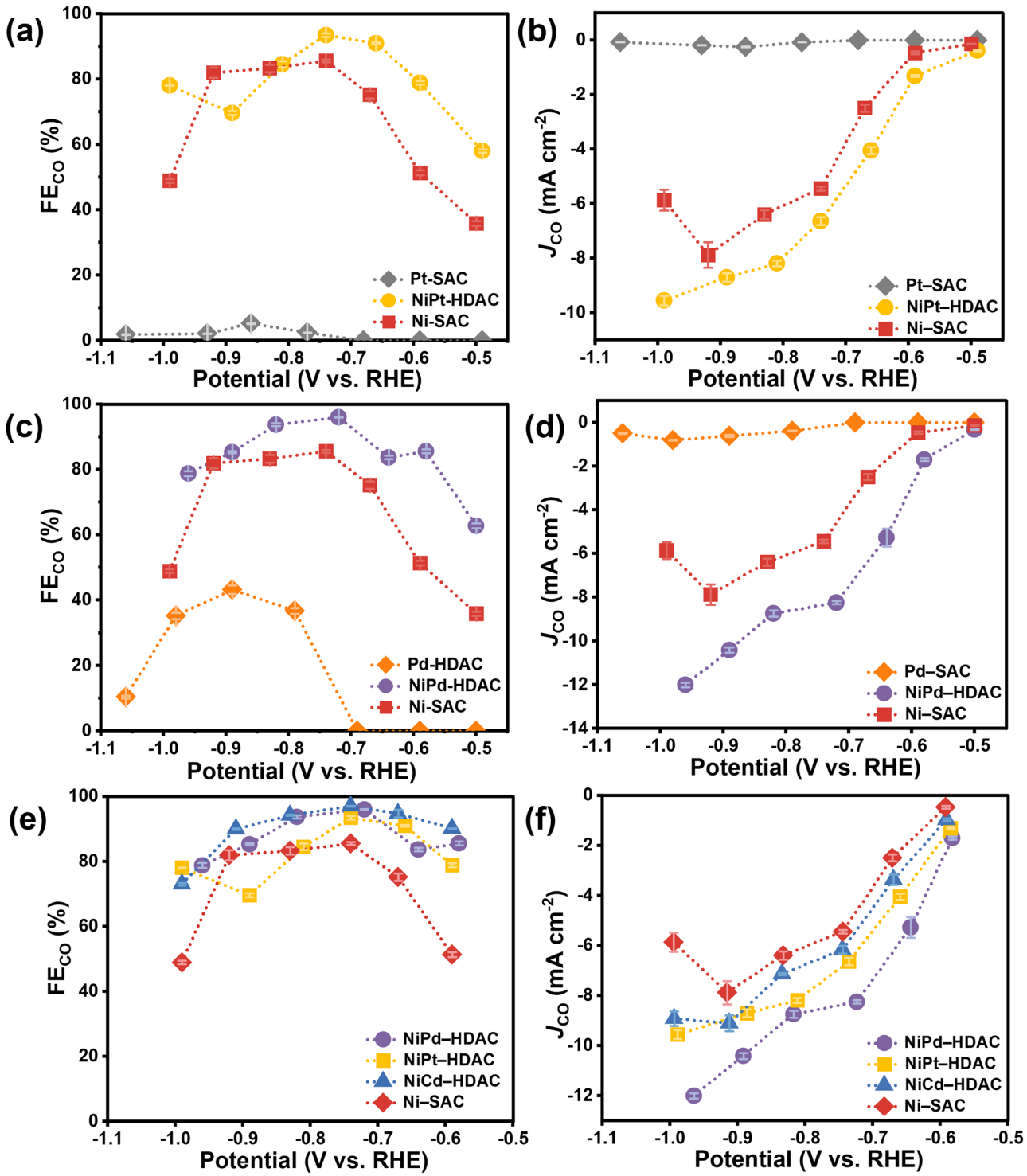

Fig. 7 | ECR performance on different NiM–HDAC (M = Cd, Pt, and Pd). a CO FEs and (**b**) CO partial geometric current densities for Ni–SAC, Pt–SAC, and NiPt–HDAC at varying applied potentials. **c** CO FEs and (**d**) CO partial geometric current densities for Ni–SAC, Pd–SAC, and NiPd–HDAC at different applied biases. **e** Comparison of CO FEs and (**f**) CO partial geometric current densities among Ni–SAC, NiPd–HDAC, NiPt–HDAC, and NiCd–HDAC at varied applied potentials. The potentials applied in all panels were *iR* corrected. The average *R* with a SE from three independent measurements for Ni-SAC, NiPt-HDAC, NiPd-HDAC, and NiCd-HDAC is 8.76 ± 0.05 Ω, 9.14 ± 0.05 Ω, 8.89 ± 0.07 Ω, and 8.69 ± 0.02 Ω, respectively. Data are represented as mean ± SE from two independent measurements. Source data are provided as a Source Data file.

Discussion

We have demonstrated an H•-transfer pathway for boosted ECR on rationally designed NiM–HDAC (M = Cd, Pt, and Pd). Experiments and DFT calculations show that M is the site where H• is produced, and the resulting H• attacks CO_2 to form •COOH. •COOH is then adsorbed by Ni for subsequent electrochemical processes to yield CO. By selecting an appropriate M site with a suitable H adsorption strength, more H• can be generated, and the reaction kinetics of the catalyst are greatly promoted. The as-developed HDACs display remarkable catalytic activity and selectivity, markedly surpassing the single-atom

counterparts. The resulting FE_{CO} exceeds 90.0% over a wide voltage range from ~ − 0.6 to − 0.91 V in an H-type cell, and approaches ~ 97.4 ± 1.3% at − 500.0 mA cm^{-2} in a flow reactor on NiCd−HDAC. The FE_{CO} is further boosted to nearly 100.0% at ~ − 2.17 V (vs. Ag/Ag^+) in an H-cell using 0.5 M [Bmim]PF_6/MeCN catholyte. Our proposed reaction mechanism and catalyst design concept open possibilities for developing highly active and selective CO_2-to-CO conversion electrocatalysts with a high atom economy. Further work in promoting C_{2+} production via the ECR by utilizing such an H•-transfer approach is underway.

Methods

Chemicals and materials

All chemicals employed in this work were analytical grade and used without further purification. Nickel acetate tetrahydrate (99.0%), cadmium nitrate tetrahydrate (99.0%), 1,10-phenanthroline (99.0%), and melamine (99.0%) were bought from Alfa Aesar. Nitric acid (65.0–68.0%), ethanol (99.7%), and hydrogen chloride solution (37.0%) were provided by Beijing Chemical Works. Palladium chloride (99.0%), ammonium fluoride (99.0%), acetonitrile (99.0%), ammonium chloride (99.0%), silver nitrate (99.0%), sodium hydroxide (98.0%), DMPO (> 97.0%), and carbon black (VXC 72 R) were acquired from Aladdin. *t*-BuOH (99.0%) was procured from Macklin. Tetraammineplatinum dinitrate (99.0%) was acquired from Adamas. Nafion solution (5.0 wt% in a mixture of water and lower aliphatic alcohols), sodium tetrachloroaurate (III) dihydrate (99.0%), sodium sulfite (99.0%), and sodium thiosulfate pentahydrate (99%) were supplied by Sigma-Aldrich. The ionic liquid [Bmim]PF_6 (99.0%) was purchased from the Lanzhou Institute of Chemical Physics, Chinese Academy of Sciences. Toray carbon paper (TGP-H-060), with a thickness of 0.19 mm, resistivity of ~ 5.8 mΩ•cm, and porosity of 78.0% as used in H-type cells; Freudenberg carbon paper (H23C9) with a thickness of 0.255 mm, resistivity of ~ 10 mΩ•cm, and 40.0% PTFE binder as used in flow cells; and Nafion 117 membranes (0.18 mm thick, ≥ 0.9 meq g^{-1} exchange capacity) were supplied by Alfa Aesar. Ultrapure water (18.2 MΩ·cm) was obtained from a Millipore system for preparing the sample solutions electrolytes, and for washing. Potassium hydroxide (99.7%), potassium chloride (99.99%), and potassium bicarbonate (99.99%) were obtained from Macklin. Deuterium oxide (D_2O for NMR, ≥ 99.9% atom D) was bought from Innochem Co., Ltd. High-purity Argon (99.999%) and carbon dioxide (99.999%) gases were purchased from Beijing Haipu Gas Co., Ltd. Carbon monoxide (99.999%) was acquired from Air Liquide (China) Holding Co., Ltd. Ag/AgCl (in saturated KCl solutions) reference electrode, 0.01 M $AgNO_3$ in 0.1 M tetra-*n*-butylammonium perchlorate-MeCN Ag/Ag^+ reference electrode, platinum wire counter electrode, platinum mesh counter electrode, and platinum foil counter electrode, were purchased from GaossUnion Co., Ltd. MFC CS200-A mass flow controllers were procured from Sevenstar Flow Co., LTD.

Synthesis of Ni−SAC, Cd−SAC, and NiCd−HDAC

Under bath ultrasonication, 1.0 g of carbon black was dispersed in 150.0 mL of 5.0 M HNO_3 solution and then heated at 90.0 °C for 4.0 h under reflux. After repeated washing with water to ensure a pH of about 7.0, the acid-treated carbon black was vacuum-dried. 0.024 mmol of nickel acetate tetrahydrate, 0.24 mmol of cadmium nitrate tetrahydrate, and 0.552 mmol of 1,10-phenanthroline hydrate were dispersed in 5.0 mL of ethanol and stirred for 1.0 h at room temperature. Then 120.0 mg of acid-treated carbon black and 240.0 mg of melamine were added to the solution and stirred for 4.0 h at 60.0 °C. Subsequently, the mixture was dried at 60.0 °C overnight. The resulting sample was annealed at 750.0 °C for 2.0 h with a ramp rate of 5.0 °C/min under an N_2 atmosphere. As a result, NiCd−HDAC with a Ni content of 0.74 wt% and Cd content of 1.66 wt% determined by ICP measurements was obtained. For the preparation of Ni−SAC and Cd−SAC, only the Ni or Cd precursor was added while the other conditions were kept constant as those used for the synthesis of NiCd−HDAC. When 0.012 mmol or 0.03 mmol of nickel acetate tetrahydrate precursor was added, NiCd−HDAC samples with a Ni content of 0.49 wt% and Cd content of 1.52 wt%, and Ni content of 0.86 wt% and Cd content of 2.13 wt% were obtained, respectively. They were denoted as corresponding NiCd (Ni: 0.49 wt%) and NiCd (Ni: 0.86 wt%).

Synthesis of Pt−SAC and NiPt−HDAC

0.024 mmol of nickel acetate tetrahydrate, 0.024 mmol of tetraammineplatinum dinitrate, and 0.12 mmol of 1, 10-phenanthroline hydrate were dispersed in 5.0 mL of ethanol and stirred at room temperature for 1.0 h. Subsequently, 120.0 mg of acid-treated carbon black and 240.0 mg of melamine were added to the above solution and stirred at 60.0 °C for 4.0 h. The mixture was then dried overnight at 60 °C. The resulting sample was then annealed at 750.0 °C for 2.0 h with a ramp rate of 5.0 °C/min under an N_2 atmosphere. As a result, NiPt−HDAC was obtained. For the synthesis of Pt−SAC, only the Pt precursor was added while the other conditions were kept constant as those used for the fabrication of NiPt−HDAC. By modulating the amount of tetraammineplatinum dinitrate added while maintaining the amount of nickel acetate tetrahydrate under similar synthetic procedures, NiPt−HDAC samples with different Ni-to-Pt molar ratios (e.g., Ni:Pt = 1:0.5 and Ni:Pt = 1:2) were obtained.

Synthesis of Pd−SAC and NiPd−HDAC

0.024 mmol of nickel acetate tetrahydrate, 0.024 mmol of palladium chloride, and 0.12 mmol of 1,10-phenanthroline hydrate were dispersed in 5.0 mL of ethanol and stirred at room temperature for 1.0 h. Subsequently, 120.0 mg of acid-treated carbon black and 240.0 mg of melamine were added to the above solution and stirred at 60.0 °C for 4.0 h. The mixture was then dried overnight at 60.0 °C. The resulting sample was then annealed at 750.0 °C for 2.0 h with a ramp rate of 5.0 °C/min under an N_2 atmosphere. As a result, NiPd−HDAC was obtained. For the synthesis of Pd−SAC, only the Pd precursor was added while the other conditions were kept constant as those used for the fabrication of NiPd−HDAC. By adjusting the amount of palladium chloride added while keeping the amount of nickel acetate tetrahydrate constant under similar synthetic procedures, NiPd−HDAC samples with different Ni-to-Pd molar ratios (e.g., Ni:Pd = 1:0.5 and Ni:Pd = 1:2) were obtained.

Catalyst characterization

X-ray powder diffraction (XRD) was performed using a D/MAX-RC diffractometer operated at 100.0 mA, 30.0 kV using Cu Kα radiation. X-ray photoelectron spectroscopy (XPS) was conducted using a Thermo Scientific ESCALAB 250Xi instrument. The instrument was equipped with an electron flood and a scanning ion gun. Spectra were calibrated against the C 1 s binding energy at 284.8 eV. Optical absorbance was obtained by a Persee TU-1950 UV-vis spectrophotometer. The Cd K-edge and In K-edge X-ray absorption near-edge structure (XANES) and extended X-ray absorption fine structure (EXAFS) spectra were measured at BL01C at the Taiwan Light Source, NSRRC. The energy resolution ($\Delta E/E$) for incident X-ray photons was found to be approximately 1.4×10^{-4} eV using a Si(111) double crystal monochromator. The Cd and In measurements were done in the fluorescence mode. Transmission electron microscopy (TEM) and aberration-corrected high-angle annular dark-field scanning TEM (HAADF-STEM) were performed using a JEOL ARM200 microscope at 200.0 kV accelerating voltage and with energy-dispersive X-ray spectroscopy (EDS). STEM sample preparation was achieved by depositing a droplet of suspension on a lacey carbon Cu grid. The Cd and Ni content was determined with an Agilent 5110 inductively coupled plasma-optical emission spectrophotometer. Raman spectra were obtained with a Renishaw in Via Raman microscope with a He/Ne laser at 532.0 nm.

Electrochemical measurements

Cathode preparation. For H-type cell measurements, 1.2 mg of catalyst was dispersed in 241.2 μL of a mixture of isopropanol, deionized water, and Nafion solution (5.0 wt%) with a corresponding volume ratio of 120.0:120.0:1.2 under bath ultrasonication for 30.0 min to attain a homogeneous suspension. The suspension was then loaded onto a Toray carbon paper working electrode with an area of 1.2 cm × 1.0 cm with a corresponding catalyst loading of 1.0 mg cm^{-2} and dried at room temperature (about 25.0 °C).

For flow cell measurements, 2.0 mg of the sample and 2.0 μL of Nafion solution (5.0 wt%) were dispersed in 400.0 μL of isopropanol/H_2O mixture under bath ultrasonication to attain a homogeneous ink. The ink was then deposited on a hydrophobic carbon paper working electrode to form catalyst films with a 1.0 mg cm^{-2} catalyst loading.

For linear sweep voltammograms in Ar- or CO_2- saturated 0.1 M $KHCO_3$ solution, 1.0 mg of a catalyst was dispersed in the mixture of 100.0 μL of ethanol, 100.0 μL of deionized water, and 100.0 μL of Nafion solution (1.0 wt%). Subsequently, the mixture was ultrasonicated for 30.0 min to yield a homogeneous ink. Then, 7.95 μL of the dispersion ink was loaded onto a 0.19625 cm^2 area glassy carbon electrode with a catalyst load of 0.135 mg cm^{-2} and dried at room temperature (about 25.0 °C).

Electrochemical CO_2 reduction tests

Salts were mixed with water or an organic solvent at the required quantity to formulate the required electrolytes, using a volumetric flask and stirring for 30 min with magnetic stir bars, then sealed to store at room temperature. The Ag/AgCl reference electrodes were calibrated against RHE with a pH = 0 high-purity H_2-saturated 0.5 M H_2SO_4, with a Pt wire as the working electrode, a graphite rod acting as the counter, and the Ag/AgCl electrode as the reference. Cyclic voltammetry was performed at a scan rate of 1.0 mV s^{-1}. The average value of the two potentials at a current of 0.0 mA was taken to be the thermodynamic potential for hydrogen evolution reaction (i.e., $E = 0.0$ V vs. RHE). The average potential for RHE was found to be − 0.197 V vs. Ag/AgCl, and therefore the calibrated potential for E (vs. Ag/AgCl) was assumed to be 0.197 V.

CO_2 electrolysis was tested in an H-type cell system with two sealed compartments of 30.0 mL for each sealed half (purchased from GaossUnion, China) separated by a Nafion 117 membrane. Before ECR tests, the Nafion membrane was pre-treated by heating in 5.0% H_2O_2 aqueous solution and 0.5 M H_2SO_4 at 80.0 °C for 1.0 h, respectively. Subsequently, the Nafion membrane was immersed in deionized water under ambient conditions for 30.0 min and then washed with deionized water. The treated membranes were kept in deionized water to prevent drying out. Toray carbon paper with a size of 1.2 cm × 1.0 cm was used as the working electrode. Pt mesh (geometric area of 1.0 × 1.0 cm^2) and Ag/AgCl (in saturated KCl solutions) electrodes were used as the counter electrode and reference electrode, respectively. The potentials were controlled by using an electrochemical working station (CHI 760E, Shanghai CH Instruments Co., China). All potentials quoted in this work were subjected to *iR* calibration and are stated relative to the RHE unless otherwise stated. The potentials in this study were measured with respect to the Ag/AgCl reference electrode (in saturated KCl solutions) and converted to the RHE reference scale by

$$E(\text{vs.RHE}) = E(\text{vs.Ag/AgCl}) + 0.197 + 0.0591\text{pH} \quad (7)$$

The electrochemical cell's resistance was measured using a potentiostatic electrochemical impedance spectroscopy (PEIS) method by scanning from 10000 Hz to 0.05 Hz both before and after the electrolysis process. The intersection of the curve with the x-axis in the EIS data denotes the solution resistance.

ECR was performed using an H-type cell (Supplementary Fig. 33) with CO_2-saturated 0.1 M $KHCO_3$ solution at room temperature (about 25.0 °C) and atmospheric pressure. The anolyte used was 12.0 mL of 0.1 M H_2SO_4 solution (unless otherwise stated) to provide sufficient protons that can migrate to the cathode through the Nafion proton exchange membrane for the CO_2 reduction reaction. When saturated with CO_2, the pH of the catholyte (12.0 mL of 0.1 M $KHCO_3$ solution) was ~ 6.81 ± 0.02. CO_2 at a flow rate of 10.0 mL·min^{-1} as controlled by a mass flow controller, was purged into the $KHCO_3$ solution for 30.0 min or more to remove any residual air in the reservoir, then controlled potential electrolysis was conducted at each potential for 60.0 min.

Linear sweep voltammetry sweeps in an Ar- or CO_2 atmosphere were performed with a 200 mL three-electrode single-compartment cell (purchased from Pine Research Instrumentation, Inc.) using Ag/AgCl as the reference, Pt wire as the counter, and glassy carbon as the working electrode, using a CHI 760E potentiostat (CHI 760E, Shanghai CH Instruments Co., China). This was done at room temperature (about 25.0 °C) and atmospheric pressure. Rotating disk electrode (RDE) experiments were run on an AFMSRCE RDE control system (Pine Inc., USA). 160.0 mL of 0.1 M $KHCO_3$ solution purged with Ar or CO_2 for at least 30.0 min was used as the electrolyte.

ECR tests were conducted at room temperature (around 25.0 °C) and pressure with an electrochemical flow cell (Supplementary Fig. S34) that consists of gas, cathodic, and anodic chambers. The working electrode was fixed between the gas and cathodic chamber, with the catalyst layer facing the cathodic chamber. An anion-exchange membrane separated the cathode and anode compartments in the flow cell. An Ag/AgCl electrode (in saturated KCl solutions) and Pt foil (geometric area: 1.5 × 3.5 cm^2) were used as the reference and counter electrode, respectively. 1.0 M KOH was the electrolyte for both compartments. Electrolytes were pumped through the catholyte and anolyte chambers with two peristaltic pumps at an equivalent flow rate of 3.0 mL min^{-1}. CO_2 gas was fed into the chamber behind the cathode at a flow rate of 20.0 mL min^{-1}, controlled by a mass flow controller.

Quantitative analysis of gas and liquid products

Gaseous products from the cell were measured with an Agilent 7890B gas chromatography (GC) system equipped with two thermal conductivity detectors (TCDs) and one flame ionization detector (FID). 20.0 mL of the gas products in the dead volume of a gas bag (~ 1.0 L) was injected into the GC with the same pressure, temperature, and time, using a sample lock syringe. CO and H_2 molar fractions of injected samples were attained based on the GC calibration curve. Liquid products were measured by ^{1}H nuclear magnetic resonance (NMR Bruker Avance III 400 HD spectrometer) by a solvent pre-saturation technique to suppress the water peak. Samples for NMR were prepared by mixing 0.5 mL of the product-containing electrolyte and 0.1 mL of DMSO-d_6 (as an internal standard). The FE values of the gas products were calculated via the below equation:

$$\text{FE} = \text{Z} \times \text{n} \times \text{F}/Q_{total} = x_i \times \upsilon \times \frac{ZFP_o}{RTI_{total}} \times 100\% \quad (8)$$

where Z is the electrons transferred count (Z equals 2.0 for CO and H_2 production), n is the number of moles of a given product, F is Faraday's constant (96485.0 C·mol^{-1}), Q_{total} corresponds to the total charge passed during the electrolysis, P_o is the atmospheric pressure, υ is the gas flow rate at the cathode gas outlet, x_i is the volume fraction of gas product i, T is the temperature, R is the ideal gas constant, and I_{total} is the total current.

The TOF for CO with different catalysts was calculated as follows[4,50]:

$$\text{TOF} = \frac{J_{CO}/ZF}{m_{cat.} \times \omega/M} \times 3600 \quad (9)$$

where J_{CO} is the partial current for the CO product, $m_{cat.}$ is the catalyst mass on the electrode, ω is the metal loading in a catalyst from ICP-AES, and M represents the atomic mass of Ni (58.69 g mol^{-1}) for the Ni-based catalysts here.

Operando EPR tests

The EPR spectra were attained using an EPR spectrometer (Japan JEOL, JES-FA300) operating in an X band frequency of 9220.531 MHz at 110.0 K. The sweep width, center field, and sweep time are 100.0 G, 3290.0 G, and 1.0 min, respectively. The operando EPR tests were conducted using a three-electrode system in an H-cell of 10 mL (purchased from GaossUnion, China) separated by a Nafion 117 membrane at room temperature, with Ag/AgCl (in saturated KCl solutions) and a Pt mesh (geometric area: 1.0 × 1.0 cm^2) as reference and counter electrodes, respectively. The catalyst loaded on CP was used as the working electrode. Before the ECR test, 6.0 mL of electrolyte saturated with purified Ar or CO_2 was mixed with 60.0 µL of DMPO, and the purified Ar or CO_2 with a flow rate of 20.0 mL min^{-1} regulated by a digital mass flow controller was fed continuously during the experiments to ensure sufficient Ar or CO_2 supply. After the ECR test was conducted at − 0.6 V (vs. RHE, without *iR* compensation), we sampled 30.0 µL of the resulting solution into a quartz standard sampling tube and sealed the bottom of the tube with a wax sealing plate, and then put the sampling tube in an EPR specific sample tube to detect H• and •COOH.

Preparation of working electrodes for SEIRAS

The gold film underlayers were pre-deposited onto silicon ATR crystal by chemical deposition. The prism was first polished with a 0.05 µm Al_2O_3 slurry and ultrasonicated in acetone and then water. The reflecting plane of the prism was then immersed in a 40.0% NH_4F solution for 5.0 min to form a hydrogen-terminated surface. The prism was subsequently immersed into a mixture of 2.0% HF and gold plating solution comprising 5.75 mM $NaAuCl_4{\cdot}2H_2O$, 0.025 M NH_4Cl, 0.025 M $Na_2S_2O_3{\cdot}5H_2O$, 0.075 M Na_2SO_3, and 0.026 M NaOH at 60.0 °C for 10.0 min. The resulting gold film on the silicon prism was rinsed with de-ionized water and dried under ambient conditions. The gold film was activated with potential scans from − 0.2 to 1.5 V (vs. RHE) in 0.1 M $NaHCO_3$ at a scan rate of 100.0 mV s^{-1} in order to improve surface enhancement. The NiCd-HDAC electrodes were prepared by dropping NiCd-HDAC ink onto the activated gold film. NiCd-HDAC ink was prepared by dispersing 100.0 mg of NiCd-HDAC powder into 2.5 mL of isopropanol, followed by adding 40.0 µL of 5% Nafion solution to the mixture. Following ultrasonication for 30.0 min, 75.0 µL of the ink was dropped onto a 1.0 cm^2 gold film, followed by drying at room temperature overnight.

Operando ATR-FTIR experiments

A custom-designed spectro-electrochemical cell with a three-electrode configuration was used for operando SEIRAS (Fig. 6a). A gold-supported NiCd-HDAC electrode was used as the working electrode, a graphite rod as the counter, and a 3.5 M KCl Ag/AgCl as the reference electrode. The cell was integrated into the Bruker INVENIO FTIR spectrometer with a liquid-nitrogen-cooled mercury cadmium telluride detector. The cell potential was controlled by a Biologic SP150 potentiostat. Spectra were recorded at a 4.0 cm^{-1} spectral resolution, and correspond to 64 co-added scans. CO_2 was kept bubbling into the electrolyte throughout, and the system was mechanically stirred. Gas flow rates were controlled by mass flow controllers (SevenStar) and calibrated with an Agilent ADM2000 universal flow meter.

For switching experiments between CO_2 and CO, CO_2 was introduced first into the electrolyte to saturate it. Then, spectral measurements were performed at a constant applied potential of − 0.9 V (vs. RHE, without *iR* compensation). The spectra were collected while the peak area remained almost unchanged during the spectral sampling. The atmosphere was then switched to CO, and spectral scanning started immediately until the peak area remained almost unchanged. Following the spectral scans, the CO atmosphere was cycled back to CO_2 and spectral scanning immediately restarted and continued until the peak area remained almost unchanged.

Computation methods

DFT calculations were carried out using the Quantum Espresso package and ultrasoft pseudopotentials[51,52]. The revised Perdew–Burke–Ernzerhof (RPBE) functional[53] was used to approximate the exchange-correlation interaction, and a plane-wave basis set with an energy cutoff of 50.0 Ry was employed. The Fermi-level smearing width was set to 0.1 eV for both geometry optimization and calculation of reaction energetics. To specifically discuss the electrocatalysis on the NiM–HDAC (M = Cd, Pt, or Pd) catalysts, we considered various $NiMN_x$ configurations in the (6 × 6) graphene slab (Supplementary Figs. S1–S3 and Supplementary Table S1). A vacuum layer as large as 16.0 Å was used along the direction normal to the surface to avoid periodic interactions. The Brillouin zone was sampled using 3 × 3 × 1 Monkhorst-Pack *k*-point grids. Spin-polarizations were considered on all calculations, and all structures were optimized until force components were below 0.05 eV/Å. The reaction free energy was calculated as $\Delta G = \Delta E_{DFT} + \Delta ZPE - T\Delta S$, where ΔE_{DFT} represents the change in total energy obtained by DFT calculations, and ΔZPE and $T\Delta S$ are the zero-point energy and entropy corrections for the gas-phase molecules taken from reference, respectively[54]. pCOHP curves were calculated by using the LOBSTER package[55]. These orbital-pair interactions can provide a quantitative measure of bond strengths. The positive and negative energy regions in the pCOHP curves correspond to the bonding and antibonding states, respectively. The vibrational modes and infrared intensities of *COOH and *COOD adsorbates were computed using a finite difference (FD) method, as implemented in the Atomic Simulation Environment (ASE) package demonstrated in recent literature[56,57].

Data availability

The data generated in this study are provided in the Supplementary Information/Source Data file. Source data are provided in this paper.

References

1. Sun, Z., Ma, T., Tao, H., Fan, Q. & Han, B. Fundamentals and challenges of electrochemical CO_2 reduction using two-dimensional materials. *Chem* **3**, 560–587 (2017).
2. Gao, S. et al. Partially oxidized atomic cobalt layers for carbon dioxide electroreduction to liquid fuel. *Nature* **529**, 68–71 (2016).
3. Phil, D. L. et al. What would it take for renewably powered electrosynthesis to displace petrochemical processes? *Science* **364**, eaav3506 (2019).
4. Zhu, J. et al. Quasi-covalently coupled Ni–Cu atomic pair for synergistic electroreduction of CO_2. *J. Am. Chem. Soc.* **144**, 9661–9671 (2022).
5. Yin, Z. et al. Cu_3N nanocubes for selective electrochemical reduction of CO_2 to ethylene. *Nano Lett.* **19**, 8658–8663 (2019).
6. Gao, D. et al. Designing electrolyzers for electrocatalytic CO_2 reduction. *Acta Phys. Chim. Sin.* **37**, 2009021 (2021).
7. Hao, L. & Sun, Z. Metal oxide-based materials for electrochemical CO_2 reduction. *Acta Phys. Chim. Sin.* **37**, 2009033 (2021).
8. Li, X. et al. Strategies for enhancing electrochemical CO_2 reduction to multi-carbon fuels on copper. *Innov. Mater.* **1**, 100014 (2023).
9. Li, S. et al. p-Block indium single-atom catalyst with low-coordinated In–N motif for enhanced electrochemical CO_2 reduction. *ACS Catal.* **12**, 7386–7395 (2022).
10. Geng, Z. et al. Oxygen vacancies in ZnO nanosheets enhance CO_2 electrochemical reduction to CO. *Angew. Chem. Int. Ed.* **57**, 6054–6059 (2018).

11. Shi, R. et al. Efficient wettability-controlled electroreduction of CO_2 to CO at Au/C interfaces. *Nat. Commun.* **11**, 3028 (2020).
12. Su, X., Yang, X.-F., Huang, Y., Liu, B. & Zhang, T. Single-atom catalysis toward efficient CO_2 conversion to CO and formate products. *Acc. Chem. Res.* **52**, 656–664 (2019).
13. Yin, J. et al. The built-in electric field across FeN/Fe_3N interface for efficient electrochemical reduction of CO_2 to CO. *Nat. Commun.* **14**, 1724 (2023).
14. Ren, W. et al. Isolated diatomic Ni-Fe metal–nitrogen sites for synergistic electroreduction of CO_2. *Angew. Chem. Int. Ed.* **58**, 6972–6976 (2019).
15. Wang, X. et al. Regulation of coordination number over single Co sites: triggering the efficient electroreduction of CO_2. *Angew. Chem. Int. Ed.* **57**, 1944–1948 (2018).
16. Jia, M. et al. Carbon-supported Ni nanoparticles for efficient CO_2 electroreduction. *Chem. Sci.* **9**, 8775–8780 (2018).
17. Hossain, M. D., Huang, Y., Yu, T. H., Goddard, W. A. III & Luo, Z. Reaction mechanism and kinetics for CO_2 reduction on nickel single atom catalysts from quantum mechanics. *Nat. Commun.* **11**, 2256 (2020).
18. Zeng, J. S., Corbin, N., Williams, K. & Manthiram, K. Kinetic analysis on the role of bicarbonate in carbon dioxide electroreduction at immobilized cobalt phthalocyanine. *ACS Catal.* **10**, 4326–4336 (2020).
19. Hu, X. et al. Boosting industrial-level CO_2 electroreduction of N-doped carbon nanofibers with confined tin-nitrogen active sites via accelerating proton transport kinetics. *Adv. Funct. Mater.* **33**, 2208781 (2023).
20. Wang, X. et al. Proton Capture Strategy for Enhancing Electrochemical CO2 Reduction on Atomically Dispersed Metal–Nitrogen Active Sites**. *Angew. Chem. Int. Ed.* **60**, 11959–11965 (2021).
21. Wang, R. et al. Proton/electron donors enhancing electrocatalytic activity of supported conjugated microporous polymers for CO_2 reduction. *Angew. Chem. Int. Ed.* **61**, e202115503 (2022).
22. Li, J. et al. Enhanced multi-carbon alcohol electroproduction from CO via modulated hydrogen adsorption. *Nat. Commun.* **11**, 3685 (2020).
23. Luo, M. et al. Hydroxide promotes carbon dioxide electroreduction to ethanol on copper via tuning of adsorbed hydrogen. *Nat. Commun.* **10**, 5814 (2019).
24. Lin, Y. et al. Tunable CO_2 electroreduction to ethanol and ethylene with controllable interfacial wettability. *Nat. Commun.* **14**, 3575 (2023).
25. Zhang, T., Yuan, B., Wang, W., He, J. & Xiang, X. Tailoring *H intermediate coverage on the $CuAl_2O_4$/CuO catalyst for enhanced electrocatalytic CO_2 reduction to ethanol. *Angew. Chem. Int. Ed.* **62**, e202302096 (2023).
26. Ma, W. et al. Promoting electrocatalytic CO_2 reduction to formate via sulfur-boosting water activation on indium surfaces. *Nat. Commun.* **10**, 892 (2019).
27. Zhou, Y. et al. Asymmetric dinitrogen-coordinated nickel single-atomic sites for efficient CO_2 electroreduction. *Nat. Commun.* **14**, 3776 (2023).
28. Liang, S., Jiang, Q., Wang, Q. & Liu, Y. Revealing the real role of nickel decorated nitrogen-doped carbon catalysts for electrochemical reduction of CO_2 to CO. *Adv. Energy Mater.* **11**, 2101477 (2021).
29. Ren, W. et al. Electronic regulation of nickel single atoms by confined nickel nanoparticles for energy-efficient CO_2 electroreduction. *Angew. Chem. Int. Ed.* **61**, e202203335 (2022).
30. Liu, S. et al. Elucidating the electrocatalytic CO_2 reduction reaction over a model single-atom nickel catalyst. *Angew. Chem. Int. Ed.* **59**, 798–803 (2020).
31. Fan, Z. et al. Oxygen-bridged indium-nickel atomic pair as dual-metal active sites enabling synergistic electrocatalytic CO_2 reduction. *Angew. Chem. Int. Ed.* **62**, e202216326 (2023).
32. Hao, Q. et al. Nickel dual-atom sites for electrochemical carbon dioxide reduction. *Nat. Synth.* **1**, 719–728 (2022).
33. Yang, H. et al. Carbon dioxide electroreduction on single-atom nickel decorated carbon membranes with industry compatible current densities. *Nat. Commun.* **11**, 593 (2020).
34. Pu, T. et al. Dual atom catalysts for energy and environmental applications. *Angew. Chem. Int. Ed.* **62**, e202305964 (2023).
35. Jafarzadeh, M. & Daasbjerg, K. Rational design of heterogeneous dual-atom catalysts for CO_2 electroreduction reactions. *ACS Appl. Energy Mater.* **6**, 6851–6882 (2023).
36. Sun, Z. et al. High-quality functionalized few-layer graphene: facile fabrication and doping with nitrogen as a metal-free catalyst for the oxygen reduction reaction. *J. Mater. Chem. A* **3**, 15444–15450 (2015).
37. Wu, Y. et al. Boosting CO_2 electroreduction over a cadmium single-atom catalyst by tuning of the axial coordination structure. *Angew. Chem. Int. Ed.* **60**, 20803–20810 (2021).
38. Han, L. et al. A single-atom library for guided monometallic and concentration-complex multimetallic designs. *Nat. Mater.* **21**, 681–688 (2022).
39. Li, J. et al. Efficient ammonia electrosynthesis from nitrate on strained ruthenium nanoclusters. *J. Am. Chem. Soc.* **142**, 7036–7046 (2020).
40. Kang, X. et al. Quantitative electro-reduction of CO_2 to liquid fuel over electro-synthesized metal–organic frameworks. *J. Am. Chem. Soc.* **142**, 17384–17392 (2020).
41. Dunwell, M. et al. The central role of bicarbonate in the electrochemical reduction of carbon dioxide on gold. *J. Am. Chem. Soc.* **139**, 3774–3783 (2017).
42. Sun, K. et al. Nature-inspired design of molybdenum–selenium dual-single-atom electrocatalysts for CO_2 reduction. *Adv. Mater.* **34**, 2206478 (2022).
43. Dunwell, M., Yan, Y. & Xu, B. In situ infrared spectroscopic investigations of pyridine-mediated CO_2 reduction on Pt electrocatalysts. *ACS Catal.* **7**, 5410–5419 (2017).
44. Moradzaman, M. & Mul, G. Infrared analysis of interfacial phenomena during electrochemical reduction of CO_2 over polycrystalline copper electrodes. *ACS Catal.* **10**, 8049–8057 (2020).
45. Firet, N. J. & Smith, W. A. Probing the reaction mechanism of CO_2 electroreduction over Ag films via operando infrared spectroscopy. *ACS Catal.* **7**, 606–612 (2017).
46. Katayama, Y. et al. Surface (electro) chemistry of CO_2 on Pt surface: an in situ surface-enhanced infrared absorption spectroscopy study. *J. Phys. Chem. C* **122**, 12341–12349 (2018).
47. Kim, B., Yoon, C. W., Kim, W. & Choi, W. Spectroelectrochemical investigation of the local alkaline environment on the surface-nanostructured Au for the conversion of CO_2 to CO. *J. Phys. Chem. C* **127**, 10968–10976 (2023).
48. Cui, Z., Jark-Wah Wong, A., Janik, M. J. & Co, A. C. Negative reaction order for CO during CO_2 electroreduction on Au. *J. Am. Chem. Soc.* **146**, 23872–23880 (2024).
49. Yang, D., Zhu, Q. & Han, B. Electroreduction of CO_2 in ionic liquid-based electrolytes. *The Innov* **1**, 100016 (2020).
50. Yi, J.-D., Gao, X., Zhou, H., Chen, W. & Wu, Y. Design of Co–Cu diatomic site catalysts for high-efficiency synergistic CO_2 electroreduction at industrial-level current density. *Angew. Chem. Int. Ed.* **61**, e202212329 (2022).
51. Vanderbilt, D. Soft self-consistent pseudopotentials in a generalized eigenvalue formalism. *Phys. Rev. B Condens. Matter* **41**, 7892–7895 (1990).
52. Giannozzi, P. et al. QUANTUM ESPRESSO: a modular and open-source software project for quantum simulations of materials. *J. Phys. Condens. Matter* **21**, 395502 (2009).
53. Hammer, B., Hansen, L. B. & Nørskov, J. K. Improved adsorption energetics within density-functional theory using revised Perdew-Burke-Ernzerhof functionals. *Phys. Rev. B* **59**, 7413–7421 (1999).

54. Chan, K., Tsai, C., Hansen, H. A. & Nørskov, J. K. Molybdenum sulfides and selenides as possible electrocatalysts for CO_2 reduction. *ChemCatChem* **6**, 1899–1905 (2014).
55. Maintz, S., Deringer, V. L., Tchougréeff, A. L. & Dronskowski, R. LOBSTER: a tool to extract chemical bonding from plane-wave based DFT. *J. Comput. Chem.* **37**, 1030–1035 (2016).
56. Porezag, D. & Pederson, M. R. Infrared intensities and Raman-scattering activities within density-functional theory. *Phys. Rev. B* **54**, 7830 (1996).
57. Hjorth Larsen, A. et al. The atomic simulation environment—a Python library for working with atoms. *J. Phys. Condens. Matter* **29**, 273002 (2017).

Acknowledgements

This work was supported by the National Key Research and Development Program of China (2022YFC2105900), National Natural Science Foundation of China (22372007, 22208020, 21972010), the Fundamental Research Funds for the Central Universities (No. JD2310, ZY2317, and buctrc202226), and the State Key Laboratory of Organic-Inorganic Composites (oic-202301007). M.Y. acknowledges the funding support from Hong Kong Polytechnic University (P0042711, P0049524, and P0047915), PolyU RCNN (P0048122), and Natural Science Foundation of Guangdong (P0046476).

Author contributions

Z.Y. designed and performed most of the experiments and wrote the draft. H.C. and M.Y. conducted the DFT calculations. Y.X. and B.X. helped to conduct operando ATR-FTIR measurements and analysis. X.Z. helped to perform some electrochemical measurements. S.H. conducted the STEM characterizations. T.W., P.X., Y.S., and M.L. carried out XAFS measurements and analyses. X.T. contributed to interpreting the data. X.T., L.H., L.X., A.R., and M.Y. helped polish the language. Z.S. co-wrote the paper and supervised the project.

Competing interests

The authors declare no competing interest.

Additional information

Supplementary information The online version contains supplementary material available at https://doi.org/10.1038/s41467-024-53529-2.

Correspondence and requests for materials should be addressed to Xinyi Tan, Ming Yang or Zhenyu Sun.

Peer review information *Nature Communications* thanks Guobin Wen, and the other anonymous reviewer(s) for their contribution to the peer review of this work. A peer review file is available.